Signal Detection on Two-Dimensional Intersymbol Interference Channels: Correlated Sources and Reduced Complexity Algorithms

By

YING ZHU

A dissertation submitted in partial fulfillment of
the requirements for the degree of

DOCTOR OF PHILOSOPHY

WASHINGTON STATE UNIVERSITY
School of Electrical Engineering and Computer Science

DECEMBER 2008

To the Faculty of Washington State University:

The members of the Committee appointed to examine the dissertation of YING ZHU find it satisfactory and recommend that it be accepted.

Chair

Co-Chair

ACKNOWLEDGEMENT

I would like to express my gratitude to my advisor, Dr. Benjamin Belzer and co-advisor, Dr. Krishnamoorthy Sivakumar, for their devoted guidance, continuous encouragement and support, and constructive suggestions throughout this research work.

I would like to thank my committee member, Dr. Thomas Fischer for his valuable advice and comments, which lead to significant improvements of this dissertation.

The financial support of this work from the NSF (grant CCR-0098357 and CCF-0635390) and the School of Electrical Engineering and Computer Science is gratefully acknowledged. Also, I want to thank Advanced Hardware Architectures, Inc. for the working experience and financial support they provided through the internship from May 2006 to Jan. 2007.

I also want to thank all the staff of the School of Electrical Engineering and Computer Science, for their help and support.

Finally, I especially wish to thank my dear husband, Xin Ai, and my parents for their encouragement, support, love and understanding.

SIGNAL DETECTION ON TWO-DIMENSIONAL INTERSYMBOL INTERFERENCE CHANNELS: CORRELATED SOURCES AND REDUCED COMPLEXITY ALGORITHMS

Abstract

by Ying Zhu, Ph.D.
Washington State University
December 2008

Chair: Benjamin Belzer

Co-Chair: Krishnamoorthy Sivakumar

In this dissertation, we present a novel iterative algorithm for detection of binary-valued 2D Markov Random Fields (MRFs) corrupted by 2D intersymbol interference (ISI) and additive white Gaussian noise (AWGN). We assume a first-order binary MRF as a simple model for correlated images. We also assume a 2D digital storage channel, where the MRF is interleaved before being written and then read by a 2D transducer; such channels occur in recently proposed optical disk storage systems. The detection algorithm is a concatenation of two soft-input/soft-output (SISO) detectors: an iterative row-column soft-decision feedback (IRCSDF) ISI detector, and a MRF detector. For the 2×2 averaging mask ISI channel, at a bit error rate (BER) of 10^{-5}, the concatenated algorithm achieves SNR savings up to 2.0 dB over the IRCSDF detector alone; the savings increase as the MRFs become more correlated, or as the SNR decreases. The algorithm is also fairly robust to mismatches between the assumed and actual MRF parameters.

The complexity of Bahl-Cocke-Jelinek-Raviv (BCJR) algorithms grows exponentially with the size of the ISI mask and is an important concern with their implementation. We consider BCJR-like iterative detection algorithms for 1D and 2D binary-input ISI channels with AWGN. The proposed new technique reduces the complexity of BCJR algorithms by decreasing the effective number of states in the trellis. It does particularly well for mixed phase sequence ISI masks, which have higher weights for the center taps and lower weights for the peripheral taps. Other complexity reduction techniques proposed in the literature perform poorly for such masks. Moreover, the complexity of the proposed state reduction technique is comparable to other reduced complexity techniques reported in the literature. Experimental results are provided to demonstrate the advantages of the proposed state reduction technique.

This dissertation also addresses the problem of equivalent masks for 4-ary and binary modulation at the same areal density. The ML bounds for these masks show that when the point spread function (PSF) is more spread, the performance of 4-ary modulation can be better than binary modulation on 2D ISI channels.

Contents

List of Figures

Chapter 1

Introduction and Background

To continue the historical trend of exponentially increasing storage density, two-dimensional (2D) storage techniques, wherein bits are written in 2D blocks (rather than 1D tracks), are being developed for magnetic and optical disks [1], and also for newer 3D technologies like holographic storage [2]. These new multi-dimensional storage techniques promise density and data read-write rate increases of more than an order of magnitude over current state of the art. However, 2D and 3D storage systems suffer from 2D and 3D intersymbol interference (ISI) due to the low-pass nature of the read-write system. Without effective equalization, 2D and 3D ISI will cause unacceptably high bit error rates (BERs) in next-generation magnetic and optical storage systems.

1.1 2D ISI System Model

We consider a $M \times N$ 2D signal $f(m,n)$ transmitted over the 2D intersymbol interference (ISI) channel. The received signal is

$$r(m,n) = \sum_{k} \sum_{l} h(k,l) f(m-k, n-l) + w(m,n), \tag{1.1}$$

where $0 \leq m \leq M-1$, $0 \leq n \leq N-1$, $h(k,l)$ is a finite-impulse-response 2D blurring mask, the $w(m,n)$ are zero mean i.i.d. Gaussian random variables (r.v.s) with variance σ_w^2, and the double sum is computed over the mask support region $\mathcal{S}_h = \{(k,l) : h(k,l) \neq 0\}$. The binary image pixels $f(m,n)$ take values -1 or $+1$. It is assumed that a boundary of -1 elements surrounds the data set.

The motivating application for this channel model is 2D magnetic or optical storage systems, which are subject to 2D ISI. Over the past 10 years, a number of papers (e.g., [3]-[14]) have considered the detection problem for binary images on the 2D ISI channel, under the assumption that the transmitted image pixels are independent and identically distributed (i.i.d.) and equiprobable.

MultiLevel recording was a technology developed by Calimetrics to increase the storage capacity of prerecorded and writable optical discs. MultiLevel recording refers to the use of multiple reflectivity values to encode data onto an optical disc. By using more than two levels, more information can be put into the minimum feature size [15]-[18]. The prototype system presented in [15] uses 8-level codes. The system in [19] uses ternary recording where an 8-bit binary data word is converted to a 5-symbol ternary code word. A look-up table stores a modulation/demodulation table defining the correspondence between the binary data word and the ternary code word.

Channel modeling and page-oriented optical memory detection are considered in [20]-[22]. If the recorded signal is 4-ary, for the optical detection system, to keep the same areal density as the binary systems, we can compute the corresponding 4-ary discrete point spread function (PSF). When we look at the ML bound performance for the discrete PSF, in some cases, the 4-ary is better then binary.

For M-ary signals, the complexity of the proposed ISI detector will increase exponentially. This dissertation considers reduced complexity algorithms for M-ary signals.

1.2 Markov Random Field (MRF) Detection

In the following, we refer to 2D signals as images. There are two reasons why past papers on detection for 2D ISI channels, and part of the present dissertation, focus on binary images: (1) almost all past, and virtually all present and proposed magnetic and optical disk storage devices and standards are binary, due to the physical difficulty of achieving reliable M-ary storage in magnetic or optical disks; and (2) detection of binary i.i.d. sources on 2D ISI channels remains an open problem, as no practical algorithm is known that can attain the performance of the maximum likelihood detector (whose performance at high signal-to-noise (SNR) is known [23]) for even simple 3×3 masks (such as, e.g., the 3×3

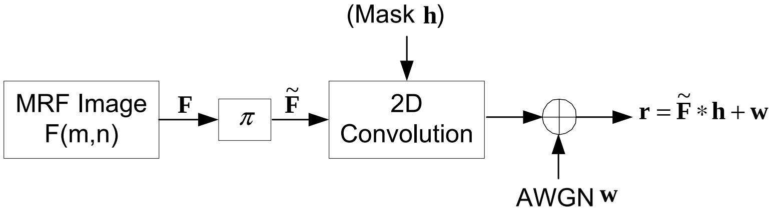

Figure 1.1: Block diagram of the assumed digital storage channel.

averaging mask where $h(k,l) = 1/9$ for $-1 \leq k, l \leq 1$). In practice, the i.i.d. assumption can be largely achieved by interleaving the original image before storage (as in Fig. 1.1), and deinterleaving it after detection. However, in practice the original image is often correlated [24, 25]. Uncompressed natural images are highly correlated; these typically occur in diagnostic medical imaging where distortion due to lossy compression is intolerable, and the time required for lossless compression/decompression may not be available. Images usually retain some correlation even if stored in compressed format, because practical lossless (or lossy) image compression schemes do not completely decorrelate the image.

We use a 2D binary MRF [26]-[28] to model the correlated source. Transmission of an $M \times N$ binary-valued 2D MRF F over the digital storage channel is shown in Fig. 1.1, where π represents an image interleaver, and $*$ represents 2D convolution. Level shifting from $\{0, 1\}$ to $\{-1, 1\}$, performed after the interleaver, is not shown. The received image

$$r(m,n) = \sum_k \sum_l h(k,l)\tilde{F}(m-k, n-l) + w(m,n), \tag{1.2}$$

where m, n, $h(k,l)$, $w(m,n)$ and the double sum have the same meaning as in (1.1), and $\tilde{F} = 2 \times \pi(F) - 1$ is an interleaved and level-shifted version of F. The MRF F takes pixel values from $\{0,1\}$, and is correlated according to the following Markov property [28]:

$$\begin{aligned} & \Pr(F_{m,n} = f_{m,n} | F_{k,l} = f_{k,l}, (k,l) \neq (m,n)) \\ = \ & \Pr(F_{m,n} = f_{m,n} | F_{k,l} = f_{k,l}, (k,l) \in \mathcal{F}_{m,n}). \end{aligned} \tag{1.3}$$

In (1.3), $F_{m,n}$ denotes pixel (m,n) of the MRF, $f_{k,l}$ denotes a particular value of pixel (k,l), and $\mathcal{F}_{m,n}$ denotes the first-order neighborhood of pixel (m,n): $\mathcal{F}_{m,n} = \{(m,n-1),(m,n+1),(m-1,n),(m+1,n)\}$. The MRF F is generated by a Gibbs sampler based on the Ising model, which is characterized by a two parameter energy function. It is assumed that the detector knows the energy parameters (and therefore the complete Markov model) of the transmitted MRF. Because of the interleaver, it is assumed that the pixels in $\tilde{F}$ are i.i.d., with $\Pr\{F(m,n) = 0\} = \Pr\{\tilde{F}(m,n) = -1\} = p_0 = 1 - p_1$ for all (m,n), where the *a priori* probabilities p_0 and p_1 need not in general equal $1/2$.

In addition, a number of proposed source-channel coding schemes produce compressed output images that can be modeled with MRFs. This dissertation exploits the correlation in the source image to greatly reduce the bit error rate on 2D ISI channels.

Although the dissertation is the first to construct an iterative algorithm for MRF detection on 2D ISI channels, and to demonstrate that it works well for detection of natural binary images on 2D ISI channels, a number of previous publications on joint source channel coding have considered joint detection and decoding of one or two dimensional Markov sources on other channels, including 1D ISI channels. MRF source modeling and joint

MRF detection and channel decoding on the AWGN channel are considered in [29]-[31]; these papers model quantized natural images (or quantized image subbands) as MRFs, and propose a number of iterative source-channel decoding algorithms that perform iterative MRF estimation using an algorithm similar to the Geman and Geman (G&G) algorithm [28]. This dissertation employs a SISO version of the G&G algorithm for MRF detection, and uses the method of [29]-[31] to construct output log-likelihood ratios from the MRF detector; however, the dissertation uses a different method to incorporate the output LLRs from the 2D-ISI detector into the Gibbs energy function of the MRF detector. In addition, the dissertation accounts for non-uniform prior pixel probabilities in the MRF detector, i.e., the case $p_0 \neq p_1$, whereas in [29]-[31] the prior probabilities are implicitly assumed to be uniform because singlet cliques are not allowed in the Gibbs energy function. In [32], the trellis structure of variable-length error correcting (VLEC) source codes for discrete memoryless sources is exploited in an iterative decoding scheme wherein a SISO VLEC source decoder exchanges information with a maximum *a posteriori* (MAP) 1D-ISI equalizer, to achieve effective control of the ISI. A variable length coding (VLC) scheme for first order Markov sources is constructed in [30], and concatenated with a recursive precoder for a 1D ISI channel; the corresponding iterative decoder exchanges soft information between a SISO VLC decoder and an equalizer employing a super-trellis for the ISI channel and the precoder. In [33], the Markov structure of the indices of a vector-quantized Gauss-Markov source is exploited to construct an iterative equalization and source decoding scheme for a 1D ISI channel. The JPEG-2000 compatible image transmission scheme proposed in [34] replaces the JPEG-2000 entropy coding stage with punctured turbo codes, and then exploits the Markov structure of the bitplanes of the quantization indices to construct an iterative successive-bitplane joint source-channel decoder; simulations over the binary-symmetric (BSC) channel show that the proposed scheme significantly outperforms traditional schemes that use JPEG-2000 with entropy coding followed by a separate channel coding step.

1.3 Iterative Row-Column Soft-Decision Feedback (IRCSDF) Algorithm Review

The following material is a summary of the papers by Cheng et.al. [3, 12].

Direct maximum likelihood (ML) detection of $M \times N$ binary 2D images requires comparison of received data with 2^{MN} candidate transmitted images, and is therefore impractical even for small image dimensions. The standard Wiener filtering solution is significantly inferior to ML detection, especially at high SNR [7]. Hence, it is desirable to develop a low-complexity 2D detection algorithm that achieves or approximates the performance of 2D ML detection. For one dimensional signals, the Viterbi algorithm (VA) provides an efficient method for ML detection of ISI-corrupted data [35]. Unfortunately the VA does not generalize to two or higher dimensions. For 2D ISI, issues of scan-order, adjacency, and causality must be considered in construction of the trellis, and the mapping between input pixel sequences and trellis paths is not one-to-one. However, union bounds on the performance of 2D ML detection have been developed in [23]; these ML performance bounds are tight at high SNR, and are useful in assessing the performance of sub-optimal 2D detection algorithms.

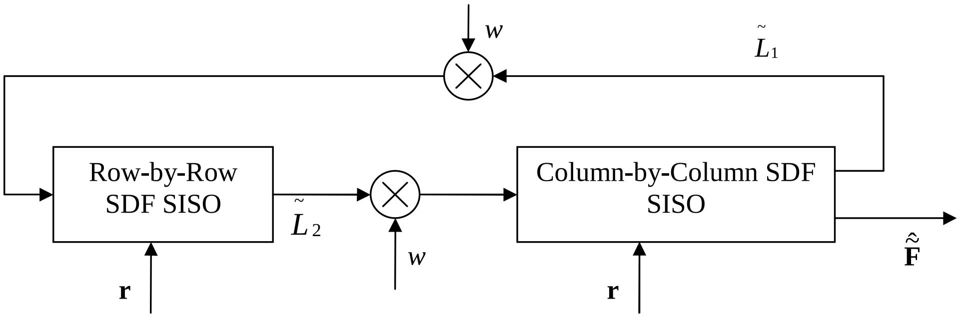

Figure 1.2: IRCSDF algorithm in a 2D ISI channel.

Figure 1.2 shows a block diagram of the algorithm scheme, in which the two estimation blocks (row-by-row, column-by-column) exchange weighted soft information. The weights w, which are less than one, prevent the algorithm from converging too quickly. Each decoder also processes received image $\mathbf{r}$, which is corrupted by 2D-ISI and by AWGN. The basic element is a *soft decision feedback, soft-input soft-output* decoder.

The IRCSDF algorithm is a modified BCJR algorithm, in which soft estimates of branch outputs and state transition probabilities from earlier trellis stages are used as *soft decision feedback* (SDF) to aid the computation of log-likelihood ratios (LLRs) for the current pixel. The SDF branch output computation computes LLRs for inner products between the mask and the image.

For the row-SISO, trellis states and inputs are defined in Figure 1.3; for the 3×3 mask, the trellis has 64-states and 8 branches entering and leaving each state. At each position

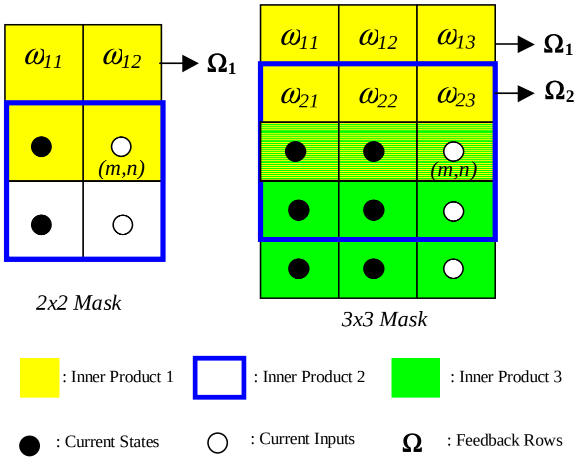

Figure 1.3: State, input, and feedback pixels for the 2×2 mask and 3×3 mask.

(m, n) the trellis branch output is a vector consisting of three 3×3 inner products between the inverted mask and the pixel values defined by the trellis; the upper inner product, named $x(m, n)$, uses two feedback rows, the middle one,named $x(m + 1, n)$, uses one feedback row and the lower one, named $x(m + 2, n)$, just uses received pixels. The branch metric is the squared Euclidean distance between the branch output and the real received pixel vector $[r(m, n), r(m + 1, n), r(m + 2, n)]$. For the 2×2 mask the trellis has 4 states and 4 branches for each state. The column-by-column case is similar to the row-by-row case.

To illustrate the SDF LLR calculation, assume the 3×3 averaging mask $h_{kl} = 1/9$ is used to compute the convolution $c(m, n) = \sum_{k=0}^{2} \sum_{l=0}^{2} f(m - k, n - l)/9$.

For pixel (m, n) at the kth stage, $k \in \{0, 1, \ldots, N\}$, the corresponding received pixel vector is $\mathbf{r} = [r(m, n), r(m + 1, n), r(m + 2, n)]$, and the actual input vector is $\mathbf{f} = [f(m, n), f(m + 1, n), f(m + 2, n)]$. To simplify, let $\mathbf{y}_k = [y_{k0}, y_{k1}, y_{k2}] = \mathbf{r}$, and $\mathbf{u} =$

$[u_{k0}, u_{k1}, u_{k2}] =$ **f**. The log-likelihood ration (LLR) is

$$L_i(k) = \log\left(\frac{P(u_{k0} = +1|\mathbf{y}_k, \tilde{\mathbf{u}}_i)}{P(u_{k0} = -1|\mathbf{y}_k, \tilde{\mathbf{u}}_i)}\right), \tag{1.4}$$

where $\tilde{\mathbf{u}}_i$ is the estimation of pixel vector **u** from decoder i, $i \in \{1, 2\}$. The extrinsic information input to decoder i is

$$\tilde{L}_i(k) = \log\left(\frac{P(u_{k0} = +1|\tilde{\mathbf{u}}_i)}{P(u_{k0} = -1|\tilde{\mathbf{u}}_i)}\right), \tag{1.5}$$

and the output extrinsic information to the next decoder is

$$\tilde{L}_{\mathrm{next}(i)}(k) = L_i(k) - \tilde{L}_i(k), \tag{1.6}$$

where $\mathrm{next}(1) = 2, \mathrm{next}(2) = 1$. By using the input extrinsic information, we can compute the conditional probability of the input pixel:

$$\begin{aligned} P(u_{k0} = +1|\tilde{\mathbf{u}}_i) &= \frac{e^{\tilde{L}_i(k)}}{1 + e^{\tilde{L}_i(k)}} \\ P(u_{k0} = -1|\tilde{\mathbf{u}}_i) &= \frac{1}{1 + e^{\tilde{L}_i(k)}}. \end{aligned} \tag{1.7}$$

Given a particular trellis state S_k, input vector **u**, and noisy received vectors $\mathbf{y}_k$, define $\lambda_k^{\mathbf{i}}(s) = P(\mathbf{u} = \mathbf{i}, S_k = s, \mathbf{y}_k)$, where $\mathbf{i} = [i_0, i_1, i_2], i_m \in \{-1, +1\}$, and $s \in \{0, 1, \ldots, 63\}$. We can then compute the *a posteriori* probability (APP)

$$P(\mathbf{u} = \mathbf{i} | \mathbf{y}_k) = \frac{\sum_s \lambda_k^{\mathbf{i}}(s)}{P(\mathbf{y}_k)}. \tag{1.8}$$

As in [36], by setting

$$\begin{aligned}
&\alpha_k(s) = P(S_k = s, \mathbf{y}_k) \\
&\beta_k(s) = P(\mathbf{y}_{k+1} | S_k = s) \\
&\gamma_{\mathbf{i}}(\mathbf{y}_k, s', s) = P(\mathbf{u} = \mathbf{i}, S_k = s, \mathbf{y}_k | S_{k-1} = s'),
\end{aligned} \tag{1.9}$$

we have

$$\begin{aligned}
\lambda_k^{\mathbf{i}}(s) &= \sum_{s'} P(\mathbf{u} = \mathbf{i}, S_k = s, S_{k-1} = s', \mathbf{y}_k) \\
&= \sum_{s'} \alpha_{k-1}(s') \gamma_{\mathbf{i}}(\mathbf{y}_k, s', s) \beta_k(s).
\end{aligned} \tag{1.10}$$

The $\alpha_k(s)$ and $\beta_k(s)$ can be computed as

$$\begin{aligned}
\alpha_k(s) &= \sum_{s'} \sum_{\mathbf{i}} \alpha_{k-1}(s') \gamma_{\mathbf{i}}(\mathbf{y}_k, s', s) \\
\beta_k(s) &= \sum_{s'} \sum_{\mathbf{i}} \beta_{k+1}(s') \gamma_{\mathbf{i}}(\mathbf{y}_{k+1}, s, s'),
\end{aligned} \tag{1.11}$$

where $\alpha_0(0) = 1, \alpha_0(s) = 0$ for $s \neq 0$; $\beta_N(0) = 1, \beta_N(s) = 0$ for $s \neq 0$. The SDF output

LLRs can be incorporated into the current pixel transition probabilities $\gamma_{\mathbf{i}}(\mathbf{y}_k, s', s)$. The modified γ is the product of a modified conditional channel PDF $p'(\cdot)$, the trellis transition probabilities, and the extrinsic information (from the other decoder):

$$\begin{aligned} &\gamma_{\mathbf{i}}(\mathbf{y}_k, s', s) \\ &= p'(\mathbf{y}_k|\mathbf{u} = \mathbf{i}, S_k = s, S_{k-1} = s') \times P(\mathbf{u} = \mathbf{i}|s, s') \\ &\times P(S_k = s|S_{k-1} = s') \times P(\tilde{\mathbf{u}}|\mathbf{u} = \mathbf{i}). \end{aligned} \tag{1.12}$$

For the given states s', s and input $\mathbf{u}$, $P(\mathbf{u} = \mathbf{i}|s, s')$ is 0 or 1 and $P(S_k = s|S_{k-1} = s')$ is 1/8 based on the trellis. The extrinsic information can be computed as:

$$P(\tilde{\mathbf{u}}|\mathbf{u} = \mathbf{i}) = \frac{P(\mathbf{u} = \mathbf{i}|\tilde{\mathbf{u}})P(\tilde{\mathbf{u}})}{P(\mathbf{u} = \mathbf{i})}, \tag{1.13}$$

where $P(\mathbf{u} = \mathbf{i}|\tilde{\mathbf{u}})$ comes from (1.7), and $P(\tilde{\mathbf{u}}) = P(\mathbf{u} = \mathbf{i}) = 1/8$. The modified channel PDF sums over all possible values of the inner products c_{sdf} associated with state transition $s' \rightarrow s$ that are affected by past decisions:

$$\begin{aligned} &p'(\mathbf{y}_k|\mathbf{u} = \mathbf{i}, S_k = s, S_{k-1} = s') = P\big(y_{k2}|u_{k0}, u_{k1}, u_{k2}, s, s'\big) \\ &\times \Bigg[\sum_{\Omega_2} P(\Omega_2) P\big(y_{k1}|u_{k0}, u_{k1}, s, s', c_{\text{sdf2}}(\Omega_2), \Omega_2\big) \\ &\times \Bigg(\sum_{\Omega_1} P(\Omega_1) P\big(y_{k0}|u_{k_0}, s, s', c_{\text{sdf1}}(\Omega_1, \Omega_2), \Omega_1, \Omega_2\big)\Bigg)\Bigg] \end{aligned} \tag{1.14}$$

where $\mathbf{\Omega}$ denotes feedback rows, inner product $c_{\text{sdf}j}(\Omega)$ is a function of the feedback pixels, and probabilities $P(\Omega_j)$ are obtained from the feedback probabilities $P(\omega_{jl})$:

$$P(\Omega_j = \omega_{j0}, \omega_{j1}, \omega_{j2}) = \prod_{l=0}^{2} P(\omega_{jl}). \tag{1.15}$$

The probabilities $P(\omega_{jl})$ can be computed by (1.7), using feedback LLRs from previously processed rows (or columns) during the current iteration. We note that, since the original image is subject to AWGN, $p'(\mathbf{y}_k|\mathbf{u} = \mathbf{i}, S_k = s, S_{k-1} = s', c_{\text{sdf}j}(\Omega))$ are normal PDFs with mean $c_{\text{sdf}j}(\Omega)$.

Since we have vector inputs and received pixels, to estimate the pixel located on (m, n), we sum the λs over $(m + 1, n)$ and $(m + 2, n)$:

$$\lambda_k^{i0}(s) = \sum_{i1,i2} \lambda_k^{i0,i1,i2}(s). \tag{1.16}$$

The pixel LLR is computed as:

$$L(k) = \log \left(\frac{\sum_s \lambda_k^{i0=+1}(s)}{\sum_s \lambda_k^{i0=-1}(s)} \right). \tag{1.17}$$

If $L(k) > 0$, we decide that pixel (m, n) is $+1$; otherwise, it is detected as -1.

1.4 Reduced Complexity BCJR Algorithms Review

The computational complexity of the BCJR-based SISO iterative algorithms grows exponentially with the size of the channel impulse response, or “mask” [37, 38]. To reduce complexity, a number of reduced-state BCJR algorithms have been proposed, including, e.g., the reduced state BCJR (RS-BCJR) of [39], the (quite similar) RS-SISO algorithm of [40], the minimum sequence metric reduced-state SISO (MSM RS-SISO) of [40], and the M-BCJR algorithm of [41]. These algorithms, when used for equalization of finite-length 1D ISI channels, typically perform reasonably close to their corresponding full-state versions when the channels are minimum- or maximum-phase. However, their performance suffers with mixed-phase channels that have relatively high-magnitude center taps and lower magnitude peripheral taps; we refer to such channel masks as “center-weighted,” and will discuss the algorithms for this type of channel in both 1D and 2D in chapter 3.

Consider the finite-length ISI channel

$$\mathbf{r} = \mathbf{h} * \mathbf{a} + \mathbf{w}, \tag{1.18}$$

where $\mathbf{h}$ is the channel mask, $\mathbf{a}$ is the data, $\mathbf{w}$ contains i.i.d. Gaussian random variables of 0 mean and variance $N_0/2$, and “*” indicates 1- or 2-dimensional convolution. For the 1D case, $\mathbf{h} = \{h_i\}$, $0 \leq i \leq L-1$, and $\mathbf{a} = \{a_k\} \in \{-1, 1\}$, $0 \leq k \leq N-1$. For 2D, $\mathbf{h} = \{h_{i,j}\}$, $0 \leq i, j \leq L-1$, and $\mathbf{a} = \{a_{k,l}\}$, $0 \leq k, l \leq N-1$. At the kth input symbol, the input to the 1D ISI channel is a_k, and the state is the previous $L-1$ symbols $a_{k-1}, \ldots, a_{k-L-1}$. This leads to a trellis diagram with 2^{L-1} states and two branches leaving (and entering) each state.

At each trellis stage in its forward pass, the M-BCJR algorithm of [41] selects the M states with the highest forward state probabilities $\alpha(m)$ and retains only those states and their connecting branches. The backward pass only considers the states and branches selected during the forward pass.

1.5 Main Contributions

In this dissertation, we present new iterative equalization schemes, which exchange soft bit estimates, resulting in significantly lower BERs than previously proposed algorithms. In particular, new algorithms for joint 2D random field estimation and ISI equalization have been developed, in order to exploit the correlation present in many 2D data blocks. On the 2×2 averaging-mask ISI channel, the proposed algorithm achieves SNR savings of up to 2.0 dB or 37% over previous detectors which do not account for correlations within data blocks. Higher SNR savings can be achieved for more correlated data blocks. The computational complexity of the proposed algorithm is comparable to that of previously published algorithms. The proposed algorithm is also robust against mismatches in the correlation parameters, thereby eliminating the need for a good model estimator.

We present a new 1D and 2D truncated state SISO algorithm. The new algorithm, based on the MSM RS-SISO of [40], uses a truncation scheme more appropriate for center-weighted masks. Simulation results show that the new algorithm significantly outperforms

MSM RS-SISO for center weighted masks.

We compare the equivalent masks for 4-ary and binary modulation at the same areal density. In some cases, binary modulation has better performance. In other cases, 4-ary modulation does better. We also considered the simulation of the row-column soft-decision feedback algorithm described in section 1.3 with 4-ary modulation, and with binary modulation and large masks. Because the trellis has more states and more branches for 4-ary modulation and/or larger size masks, reduced complexity algorithms are needed to simulate the system with these masks.

1.6 Dissertation Outline

The rest of this dissertation is organized as follows. In chapter two, the detection of Markov random fields on 2D ISI channels is presented. The material of this chapter was partially presented at the 44th Annual Allerton Conference on Communication, Computing, and Control in September 2006 [42] and journal article of "IEEE Transactions on Signal Processing" in July 2008 [43] . In chapter three, we consider the reduced state BCJR algorithms for one- and two-dimensional equalization. The material of this chapter was partially presented at the IEEE International Conference on Acoustics, Speech and Signal Processing in Mar./Apr. 2008 [44]. In chapter four, we give the masks for binary and 4-ary modulation with both Gaussian and Sinc square PSFs. Also in chapter four the reduced complexity algorithms are discussed. Finally, the dissertation is concluded in chapter five.

Chapter 2

Markov Random Field Detection on Two-Dimensional Intersymbol Interference Channels

In this chapter, we present an iterative detection scheme that exploits the correlation in the original image to achieve significant SNR savings over ISI detection schemes which do not account for correlated input images. Both the MRF detector and the ISI detector in our technique account for non-uniform prior probabilities, and we demonstrate the iterative detection scheme on non-uniformly distributed natural binary images. Although we model the image correlation by a simple first-order Markov random field, our results give at least a proof of principle that can be further explored with more realistic image models.

2.1 The Concatenated Detector

The block diagram of the digital storage channel has been shown in Fig. 1.1. A block diagram of the concatenated detection system is shown in Fig. 2.1. It operates according to the "turbo principle" (after turbo-codes [45]), whereby two or more SISO decoders exchange extrinsic information and iterate until convergence. The received image $\mathbf{r}$ is an input to the ISI detector, which attempts to remove the ISI under the assumption that the pixels of $\tilde{F}$ in Fig. 1.1 are i.i.d. The ISI detector outputs deinterleaved extrinsic log-likelihood ratios (LLRs) to the MRF detector, which estimates the original MRF F, and feeds back interleaved extrinsic LLRs to the ISI detector.

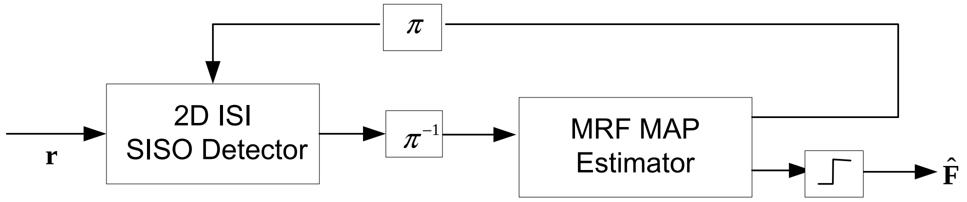

Figure 2.1: Block diagram of the concatenated detector.

Two comments are in order about how the proposed joint MRF estimator and ISI detector would fit into a digital storage system. First, although Figs. 1.1 and 2.1 do not include channel coding, it could easily be incorporated into the proposed joint detection and equalization scheme by replacing the 2D ISI SISO equalizer in Fig. 2.1 with a joint channel decoder/equalizer, and letting the decoder/equalizer exchange soft information with the MRF detector. Second, the 2D correlation assumed to exist in the source image would be very small if the source image were compressed using an entropy code. Most standard entropy codes are variable length, and their decoders suffer catastrophic failure when they encounter channel-induced bit errors. For this reason, a number of proposed source-channel coding schemes (e.g., [29, 33, 34] described in chapter 1) avoid entropy coding, and yet their end-to-end performance is competitive with entropy coded systems that employ separate source and channel coding. Hence, it is not unrealistic to assume that the proposed detection system may be part of a digital storage system that does not use entropy coding.

2.1.1 The ISI Detector

A detailed description of the ISI detector, including performance comparisons with a number of other previously published 2D ISI algorithms, appears in [3, 12] and is briefly described in Section 1.3.

The IRCSDF algorithm used in 2D ISI SISO detector consists of two SISO modules, run on rows and columns, which exchange weighted soft information estimates of the interleaved MRF $\tilde{F}$. Each module runs the BCJR algorithm [36] on several rows (columns) of the image at once, and uses soft decision feedback from previously-processed rows (columns), to arrive at an LLR estimate $\tilde{L}$ of the current row (or column.) The weight w attenuates the LLR estimates, to correct for the over-confidence effect resulting from use of SDF.

If the candidate input pixels i_j take values from $\{-1, 1\}$ with *a priori* probabilities p_0 and p_1, we use the non-equiprobable version of IRCSDF which is described in [46].

To the best of our knowledge, the above-described IRCSDF algorithm gives the best published performance for equalization of the 2×2 averaging mask on non-trivially-sized source images, with the exception of the concatenated zig-zag algorithm of [13], which uses the IRCSDF algorithm as a component. We chose the IRCSDF algorithm for the experiments described in this dissertation because it is about half as complex as the concatenated zig-zag algorithm, and because the focus in this dissertation is on the improvements provided by concatenating a MRF detector with an ISI detector.

2.1.2 The MRF Detector

The MRF detector is designed to provide a maximum *a posteriori* (MAP) estimate of the original MRF F from its noisy version $G = F + z$, where z is zero mean 2D AWGN. The MRF detector's extrinsic input LLRs are the deinterleaved extrinsic output LLRs from the ISI detector:

$$L_{\text{in}}^{\text{MRF}} = \pi^{-1}\left(L_{\text{out}}^{\text{ISI}}\right).$$

In practice, the $L_{\text{in}}^{\text{MRF}}$ are (approximately) conditionally normal, with conditional means μ_+ and μ_- corresponding to pixel values of $+1$ or -1 in $\pi^{-1}(\tilde{F})$. The MRF detector computes sample mean and variance estimates $\hat{\mu}_+$, $\hat{\mu}_-$, $\hat{\sigma}_+^2$, and $\hat{\sigma}_-^2$ for the two conditional input PDFs. The LLRs $L_{\text{in}}^{\text{MRF}}$ are then shifted and scaled to form the "noisy image" G, which has conditional means of 0 and 1:

$$G(m,n) = \frac{L_{\text{in}}^{\text{MRF}}(m,n) - \hat{\mu}_-}{\hat{\mu}_+ - \hat{\mu}_-}. \tag{2.1}$$

The conditional variances of G are estimated as

$$\sigma_G^2 = \frac{N_+\hat{\sigma}_+^2 + N_-\hat{\sigma}_-^2}{(N_+ + N_-)(\hat{\mu}_+ - \hat{\mu}_-)^2} \quad , \tag{2.2}$$

where N_+ and N_- are the number of positive and negative pixels in the input LLR image $L_{\mathrm{in}}^{\mathrm{MRF}}$.

Generation of the MRFs

The conditional probabilities in (1.3) are calculated according to the Gibbs distribution [28]

$$\Pr(F_{m,n} = f_{m,n} | F_{k,l} = f_{k,l}, (k,l) \in \mathcal{F}_{m,n}) = \frac{e^{-\mathcal{E}(f_{m,n})/T}}{\sum_{f=0}^{1} e^{-\mathcal{E}(f)/T}}. \tag{2.3}$$

The energy function $\mathcal{E}$ used to generate the MRFs in this dissertation follows the Ising model:

$$\mathcal{E}_I(f_{m,n}) = f_{m,n}(\alpha + \beta v_{m,n}), \tag{2.4}$$

where $v_{m,n} = f_{m,n-1} + f_{m,n+1} + f_{m-1,n} + f_{m+1,n}$. The MRF becomes more correlated as the interaction coefficient β becomes increasingly large and negative. Coefficient α is related to the prior probability of pixel (m,n); α is set equal to -2β when the pixels are equiprobable. The "temperature" parameter T is set to one to generate the original MRFs, but is varied according to an annealing schedule during the stochastic relaxation algorithm used for MRF estimation.

The method used to simulate the MRF is as follows[47]:

1. Start with an i.i.d. random configuration.

2. Randomly chose two pixels.

3. Compute the energy change $\Delta\mathcal{E}$ if these two pixels are switched.

4. If $\Delta\mathcal{E} < 0$, i.e., if the energy decreases, accept the switch.

5. Otherwise, accept the switch with probability $q \propto \exp(-\Delta\mathcal{E})$.

6. Go to 2) until convergence occurs.

This method ensures that the generated MRF has the same number of 0s and 1s as the initial configuration, and after the interleaver it has the same distribution as an i.i.d. source. Two examples of generated equiprobable MRFs are shown as images b and c in Fig. 2.2. In these images, black represents 0, and white represents 1. Image b has $\beta = -1.5$, and image c has $\beta = -3.0$; from the figure it is clear that image c is more correlated than image b. Fig. 2.2 (a) shows an i.i.d. image for comparison.

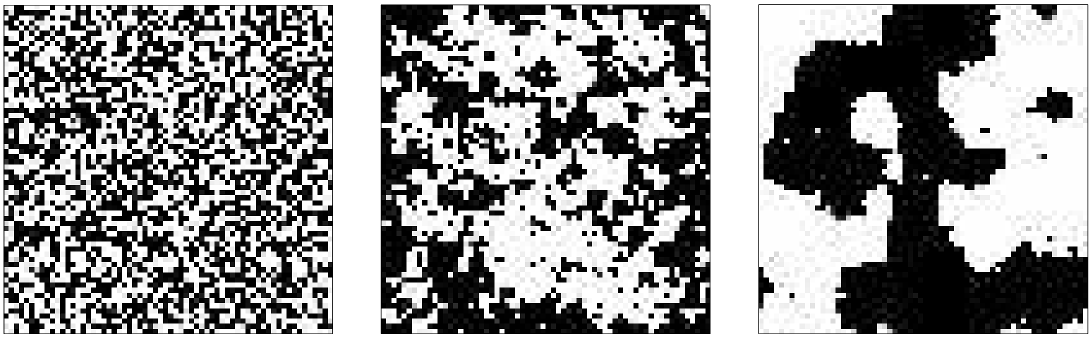

(a) (b) (c)

Figure 2.2: Three 64×64 equiprobable binary images: (a) i.i.d. image; (b) MRF with correlation parameter $\beta = -1.5$; (c) MRF with $\beta = -3.0$.

If the source image is non-equiprobable, then parameter α in the MRF model needs to be modified as follows. If we level shift the binary alphabet for $F_{m,n}$ such that $0 \to -1$

and $1 \rightarrow 1$, let $\beta = 0$, and denote the level-shifted pixels by $f'_{m,n}$, then $\mathcal{E}_I(f'_{m,n}) = f'_{m,n}\alpha_1$, where we use the notation α_1 to denote the alpha constant for the $\{-1, 1\}$ alphabet. So,

$$p_0 \equiv P(F'_{m,n} = -1) = \frac{e^{\alpha_1}}{e^{-\alpha_1} + e^{\alpha_1}}$$

$$p_1 \equiv P(F'_{m,n} = +1) = \frac{e^{-\alpha_1}}{e^{-\alpha_1} + e^{\alpha_1}},$$

which gives

$$\alpha_1 = \frac{1}{2}\log\frac{P(F'_{m,n} = -1)}{P(F'_{m,n} = +1)} = \frac{1}{2}\log\frac{p_0}{p_1}.$$

Now, we map the values from $\{-1, 1\}$ to $\{0, 1\}$ and consider the energy function in (2.4):

$$\begin{aligned}
\mathcal{E}_I(f_{m,n}) &= f'_{m,n}(\alpha_1 + \beta v'_{m,n}) \\
&= (2f_{m,n} - 1)\{\alpha_1 + \beta[(2f_{m,n-1} - 1) + (2f_{m,n+1} - 1) \\
&\quad +(2f_{m-1,n} - 1) + (2f_{m+1,n} - 1)]\} \\
&= 2\alpha_1 f_{m,n} + 4\beta v_{m,n} f_{m,n} - 8\beta f_{m,n} - 2\beta v_{m,n} + 4\beta - \alpha_1 \\
&= \frac{1}{4} f_{m,n}(\frac{1}{2}\alpha_1 - 2\beta + \beta v_{m,n}) - 2\beta v_{m,n} + 4\beta - \alpha_1 \\
&= \frac{1}{4} f_{m,n}(\alpha + \beta v_{m,n}) - 2\beta v_{m,n} + 4\beta - \alpha_1, \qquad (2.5)
\end{aligned}$$

where

$$\alpha = \frac{1}{2}\alpha_1 - 2\beta = \frac{1}{4}\log\frac{p_0}{p_1} - 2\beta. \qquad (2.6)$$

Given the neighbors $v_{m,n}$, $(-2\beta v_{m,n} + 4\beta - \alpha_1)$ is a constant which does not affect the probability computation. An example MRF with $(p_0, p_1) = (0.1, 0.9)$ is shown in Fig. 2.3.

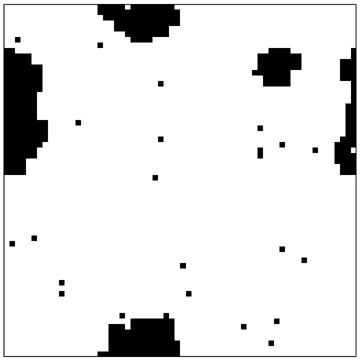

Figure 2.3: Non-equiprobable 64×64 binary MRF, with $p_0 = 0.1$ and $\beta = -3.0$.

Stochastic Relaxation

The stochastic relaxation algorithm of Geman and Geman (G&G) [28] is an iterative algorithm that proceeds at discrete time steps $t = 0, 1, 2, \ldots, t_{\max}$; after each step, a new MRF estimate $\hat{F}(t)$ is obtained. For sufficiently large $t_{\max}$, the algorithm converges to a final estimate $\hat{F}$ that does not change appreciably for $t > t_{\max}$. The initial estimate $\hat{F}(0)$ is computed by thresholding the noisy image G at $1/2$. Given estimate $\hat{F}(t)$ at time t, at time $t + 1$ $M \times N$ randomly chosen pixels of $\hat{F}(t)$ are visited. The value of each pixel (m, n) visited during the random scan is set to 0 or 1 with probability $1/2$. If the new value is different from its value $\hat{f}_{m,n}$ at time t, then the energy difference $\Delta\mathcal{E}_P(m, n) = \mathcal{E}_P(\mathrm{NOT}(\hat{f}_{m,n})) - \mathcal{E}_P(\hat{f}_{m,n})$ is computed, where $\mathcal{E}_P$ is the modified (*a posteriori*) energy function which includes the difference energy between the noisy input image

G and the current trial estimate, and is defined at time $t+1$ as:

$$\mathcal{E}_P(f_{m,n}) = \mathcal{E}_I(f_{m,n}) + \|G - \hat{F}(t, f_{m,n})\|^2/2\sigma_G^2. \tag{2.7}$$

In (2.7), $\hat{F}(t, f_{m,n})$ denotes the estimated MRF $\hat{F}(t)$ with pixel (m,n) taking the value $f_{m,n}$, and σ_G^2 is estimated as in (2.2). In computing $\Delta\mathcal{E}_P(m,n)$, only one pixel at a time (i.e., pixel (m,n)) is changed; all other pixels retain their values from time t. If $\Delta\mathcal{E}_P(m,n) < 0$, then the change is accepted: $\hat{f}_{m,n}(t{+}1) = \mathrm{NOT}(\hat{f}_{m,n}(t))$. If $\Delta\mathcal{E}_P(m,n) \geq 0$, the change is accepted with probability $q = \exp\left[-\Delta\mathcal{E}_P(m,n)/T(t+1)\right]$. The temperature T is gradually reduced according to a logarithmic annealing schedule: $T(t) = C/\log(1+t), 1 \leq t \leq t_{\max}$; in this dissertation the value $C = 3.0$ is used for all simulations.

The extrinsic information LLRs $L_{\text{in}}^{\text{MRF}}(m,n) = \log\left[\Pr_{\text{ext}}(F_{m,n}=1)/\Pr_{\text{ext}}(F_{m,n}=0)\right]$ are independent *a priori* information about pixel (m,n). Hence, in the $\mathcal{E}_I(f_{m,n})$ of (2.7), we replace α with

$$\alpha' = \alpha - L_{\text{in}}^{\text{MRF}}(m,n). \tag{2.8}$$

After converting to probabilities using (2.3), this extra LLR term in α' results in the corresponding extrinsic probabilities $\Pr_{\text{ext}}(F_{m,n} = f_{m,n})$ appearing as independent weight factors in the renormalized expressions for the conditional probabilities of (2.3). Thus, as the LLRs $L_{\text{in}}^{\text{MRF}}(m,n)$ grow increasingly large with successive iterations of the concatenated detector, they increasingly influence the estimates $\hat{F}$ arrived at by the MRF detector.

The G&G algorithm provides only a binary estimate $\hat{F}$ of the MRF. To compute LLR estimates $L^{\mathrm{MRF}}(m,n)$ for each pixel, we use the following method, which is similar to that in [29, 31], where a soft-output G&G algorithm is used for recovery of noise-corrupted MRFs, and for iterative source-channel image decoding with MRF source models. After the stochastic relaxation algorithm convergence, we compute the conditional probabilities based on the MRF model:

$$\Pr(F_{m,n} = 0|\mathcal{F}_{m,n}) = \frac{1}{1 + e^{-(\alpha' + \beta v_{m,n})/T}} \tag{2.9}$$

$$\Pr(F_{m,n} = 1|\mathcal{F}_{m,n}) = \frac{e^{-(\alpha' + \beta v_{m,n})/T}}{1 + e^{-(\alpha' + \beta v_{m,n})/T}}. \tag{2.10}$$

The LLRs $L^{\mathrm{MRF}}(m,n)$ are then computed as

$$\begin{aligned} L^{\mathrm{MRF}}(m,n) &= -(\alpha' + \beta v_{m,n})/T \\ &= -\frac{(\alpha - L_{\mathrm{in}}^{\mathrm{MRF}}(m,n) + \beta v_{m,n})}{T}. \end{aligned} \tag{2.11}$$

Finally, since $L_{\mathrm{in}}^{\mathrm{MRF}}(m,n)$ is weighed by $1/T$,

$$\begin{aligned} L_{\mathrm{out}}^{\mathrm{MRF}}(m,n) &= L^{\mathrm{MRF}}(m,n) - L_{\mathrm{in}}^{\mathrm{MRF}}(m,n)/T \\ &= -(\alpha + \beta v_{m,n})/T. \end{aligned} \tag{2.12}$$

The per-pixel complexity of the proposed MRF-ISI detector is now summarized, under the assumption of a 2×2 ISI mask. (The mask size affects only the complexity of the ISI detector). Each pass through the MRF detector results in a per-pixel complexity of $10+9p_d \times N_{\text{it}}$ adds/subtracts, $3+(8p_d+p_d \times p_\Delta) \times N_{\text{it}}$ multiplies/divides, $1+p_d \times p_\Delta \times N_{\text{it}}$ exp/log operations, and $(3 + p_d \times p_\Delta) \times N_{\text{it}}$ random number generations, where $p_d = 1/2$ is the probability that the new trial pixel and the old pixel are different, p_Δ is the probability that the energy change $\Delta \mathcal{E}_P(m, n) \geq 0$, and N_{it} is the number of iterations of the stochastic relaxation algorithm. Simulation results for image (c) in Fig. 2.2 at moderate SNRs of 11 and 12 dB indicate that p_Δ is close to 1. Assuming that $p_\Delta = 1$, then the MRF detector's complexity per pixel per iteration is 10.5 adds/subtracts, 7.5 multiplies/divides, 1.5 exp/log, and 3.5 random number generations. By comparison, the MRF source decoder of [29] requires about 180 adds/subtracts per pixel per iteration, assuming the four doublet cliques used in the Ising model of the present paper (and neglecting the singlet), 1 bit source vectors, and no block coding (corresponding to the parameter settings $N_C = 4$, and $N = M = 1$ in [29]). Our technique has somewhat lower complexity because our sources are binary, so that we do not need to do the source modeling done in [29]. The ISI detector uses three-row IRCSDF, which needs 1935 adds/subtracts, 3398 multiplies/divides, and 391 exp/logs per pixel. Using the typical values $p_\Delta = 1$, and $N_{\text{it}} = 300$, five iterations of the MRF-ISI detector require a total of 16475 adds/subtracts, 23755 multiplies/divides, 2710 exp/logs, and 5250 random number generations per pixel. In these figures, the complexity due to the MRF detector is roughly equal to that of the ISI detector. The simulation results in the following section demonstrate that the approximate doubling of the complexity over

ISI detection alone can give performance gains as high as 2.5 dB at high SNR.

2.2 Simulation Results

During initial iterations of the concatenated system of Fig. 2.1, the ISI detector cannot remove all the ISI from received image **r**. Due to its use of soft-decision feedback, the ISI detector is also subject to error propagation, especially at low SNRs. Thus, the "noisy image" G supplied to the MRF detector by the ISI detector contains bit errors as well as Gaussian-like noise. To verify that the MRF detector can correct some of these bit errors (by exploiting the Markov structure of the image), we performed the simulation diagrammed in Fig. 2.4. The MRF passes through a binary-symmetric channel (BSC) with crossover probability p, followed by an AWGN channel, and is then detected with the MRF MAP estimator. Fig. 2.5 plots the BER of the hard decisions made at the MRF estimator's output versus the SNR $10\log_{10}\left(\text{var}\left[F\right]/\sigma_w^2\right)$ of the AWGN channel, for several values of the BSC error probability p. In every case, the MRF detector's output has an error floor lower than the value of p used in the simulation. This result strongly suggests that the MRF detector can improve the reliability of the information passed to it by the ISI detector.

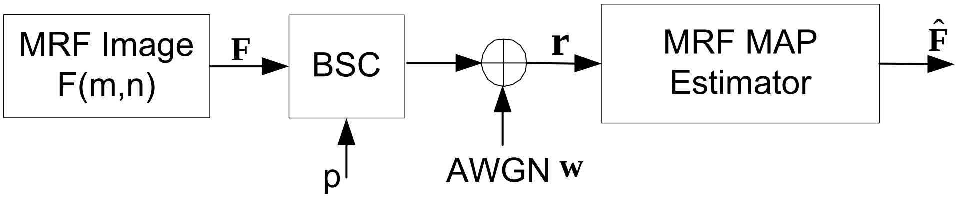

Figure 2.4: Experiment to test error correction capability of the MRF detector.

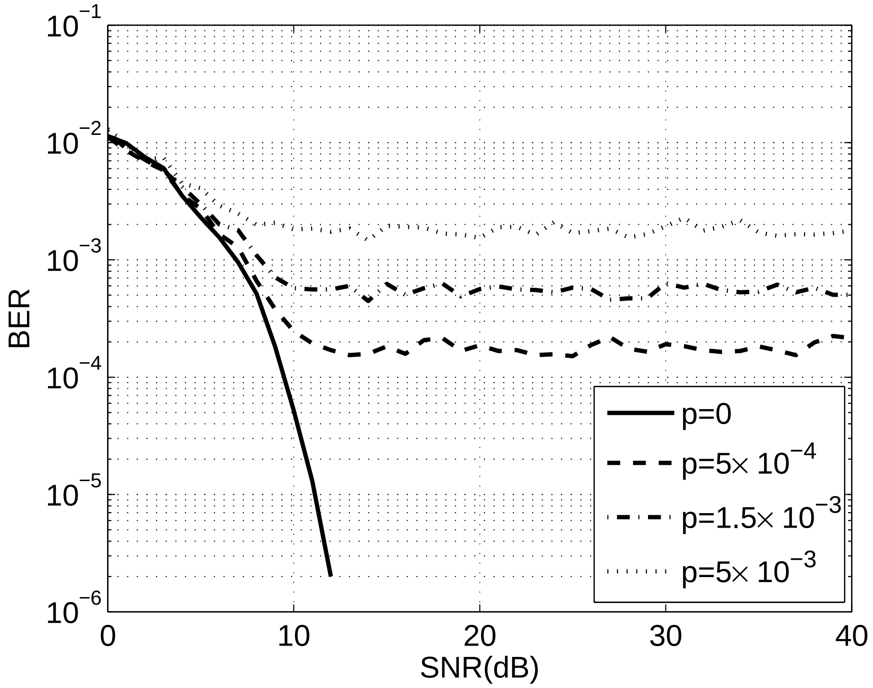

Figure 2.5: Simulation results for the experiment shown in Fig. 2.4.

Unless otherwise noted, all simulations of the concatenated system of Fig. 2.1 used the the 2×2 averaging mask (with $h(k,l) = 1/4$ for $0 \leq (k,l) \leq 1$) in the 2D convolution of (1.1). Unless otherwise noted, all simulations used 5 outer iterations of the entire concatenated system, with one inner iteration of the ISI detector performed for each outer iteration. In the following subsections, we present simulation results for three cases: (1) the source image is a binary first order MRF, and the receiver knows the MRF parameters; (2) the source image is a binary first order MRF, and the receiver guesses the MRF parameters; and (3) the source image is a natural binary image, and the receiver guesses the most appropriate MRF parameters.

2.2.1 MRF Source and Known Markov Parameters at the Receiver

Monte-Carlo simulation results for the concatenated system, when the source images were the two 64×64 binary equiprobable MRFs shown in Fig. 2.2(b) and (c), are shown in Fig. 2.6. For image (c), results for both the 2×2 and 3×3 averaging masks are shown. (The 3×3 averaging mask has $h(k,l) = 1/9$ for $-1 \leq k, l \leq 1$). The SNR in Fig. 2.6 is defined as in [12]:

$$\text{SNR} = 10 \log_{10} \left(\text{var} \left[\tilde{F} * h \right] / \sigma_w^2 \right), \tag{2.13}$$

where $*$ denotes 2D convolution, and σ_w^2 is the variance of the Gaussian r.v.s $w(m,n)$ in (1.1). The performance of the IRCSDF ISI detector alone on the received image $\mathbf{r}$ is also shown for comparison. For the 2×2 mask at a BER of 2×10^{-5}, the concatenated system gives SNR savings of 0.5 and 1.5 dB over the ISI detector alone, for images (b) and (c) respectively. As the input MRF becomes more correlated, the MRF detector makes increasingly reliable decisions, thereby improving the system's SNR gain. For the 2×2 mask at a BER of 2×10^{-3}, the concatenated system saves about 0.8 and 2.2 dB over the ISI detector alone, for images (b) and (c) respectively. The gains increase at lower SNR, where the additional input of the MRF detector helps the ISI detector resolve an increased number of ambiguous cases. For the 3×3 averaging mask at a BER of 10^{-4}, the concatenated system operating on image (c) saves about 2.5 dB over the ISI detector alone; it appears that increasing the mask size also increases the number of ambiguous cases output from the ISI detector, making the MRF detector's assistance more valuable. For the 3×3 averaging mask a total of 2 outer iterations were used, with 2 inner iterations of the ISI detector per outer iteration. Experiments indicated that this was the best iteration schedule for the 3×3 mask. Additional outer iterations beyond 2 gave no additional gains.

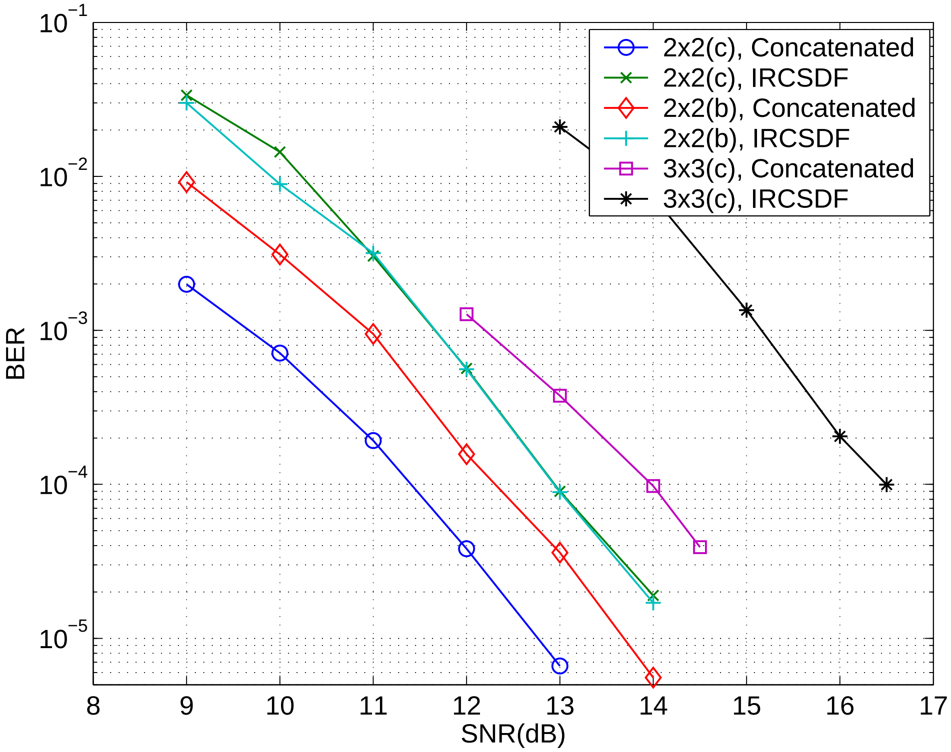

Figure 2.6: Simulation results for the concatenated system on the 2D ISI channel with 2×2 and 3×3 averaging masks, for MRFs (b) and (c) shown in Fig. 2.2. The performance of the ISI detector alone is also shown for comparison.

We also considered first order MRFs with non-equiprobable pixels. Fig. 2.7 shows simulation results on the $p_0 = 0.1$, $\beta = -3.0$ MRF of Fig. 2.3. The figure shows performance of the concatenated system, as well as the performances of the non-equiprobable and equiprobable ISI detectors alone. Non-equiprobable ISI detection offers little gain at high SNR, but saves between 0.5 and 1 dB at lower SNRs. The addition of the MRF detec-

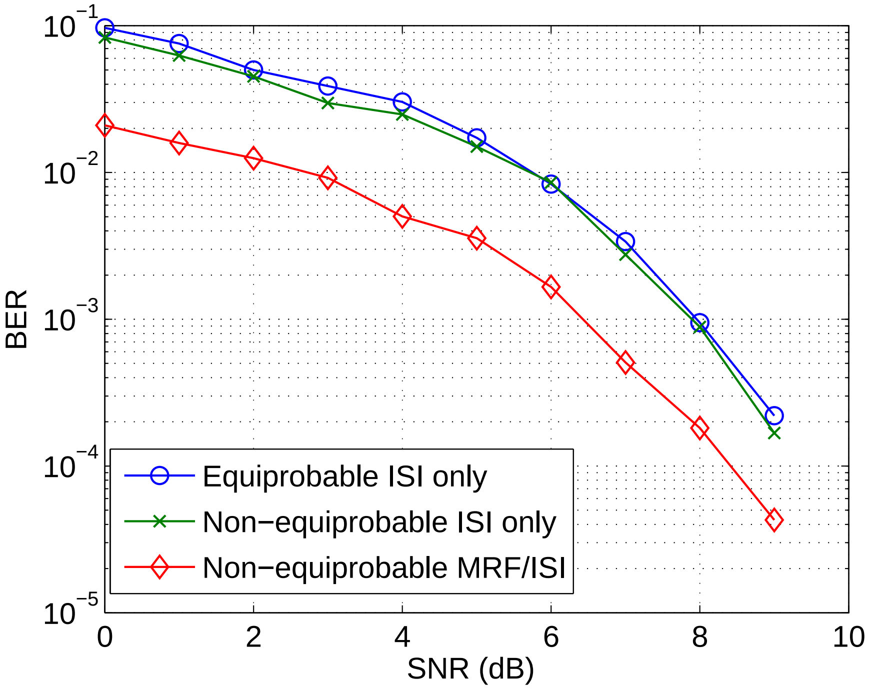

Figure 2.7: Simulation results for the concatenated system on the 2D ISI channel with 2×2 averaging mask, for the non-equiprobable MRF with $p_0 = 0.1$ and $\beta = -3.0$ shown in Fig. 2.3. The performances of the equiprobable and non-equiprobable ISI detectors alone are also shown for comparison.

tor (with modified α as in (2.6)) gives SNR savings of about 1 dB at BER 2×10^{-4}, and about 3 dB at BER 10^{-2}, over non-equiprobable ISI detection alone. A similar set of simulation results, but with $p_0 = 0.01$, is shown in Fig. 2.8. Now the gain of non-equiprobable ISI compared to equiprobable ISI detection is higher: about 0.5 dB at BER 10^{-4}. But the gain of the concatenated system over non-equiprobable ISI is smaller: about 0.3 dB at BER 2×10^{-4}. Clearly it is worth exploiting a non-uniform pixel distribution by using the non-equiprobable concatenated system in place of equiprobable ISI detection alone, although for extremely skewed distributions, non-equiprobable ISI detection alone achieves most of the available SNR gain.

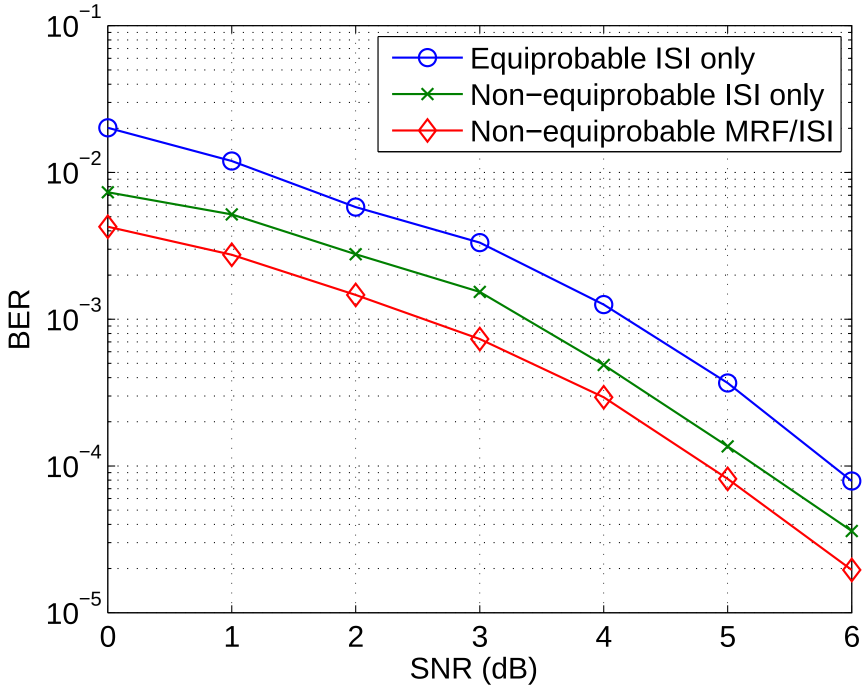

Figure 2.8: Simulation results for the concatenated system on the 2D ISI channel with 2×2 averaging mask, for a non-equiprobable MRF with $p_0 = 0.01$ and $\beta = -3.0$. The performances of the equiprobable and non-equiprobable ISI detectors alone are also shown for comparison.

It is also worth noting that the concatenated algorithm greatly outperforms the standard G&G algorithm applied to a non-interleaved MRF passed through the ISI channel. Simulation results for the G&G algorithm alone operating on a $\beta = -3.0$ MRF passed through the 2×2 averaging-mask ISI channel are shown in Fig. 2.9. The SNR in this figure is defined by replacing $\tilde{F}$ by F in (2.13). From the figure it is clear that the G&G algorithm alone has a BER floor of about 1.5×10^{-3}, and thus is not suitable for 2D digital storage applications, where much lower BERs are required.

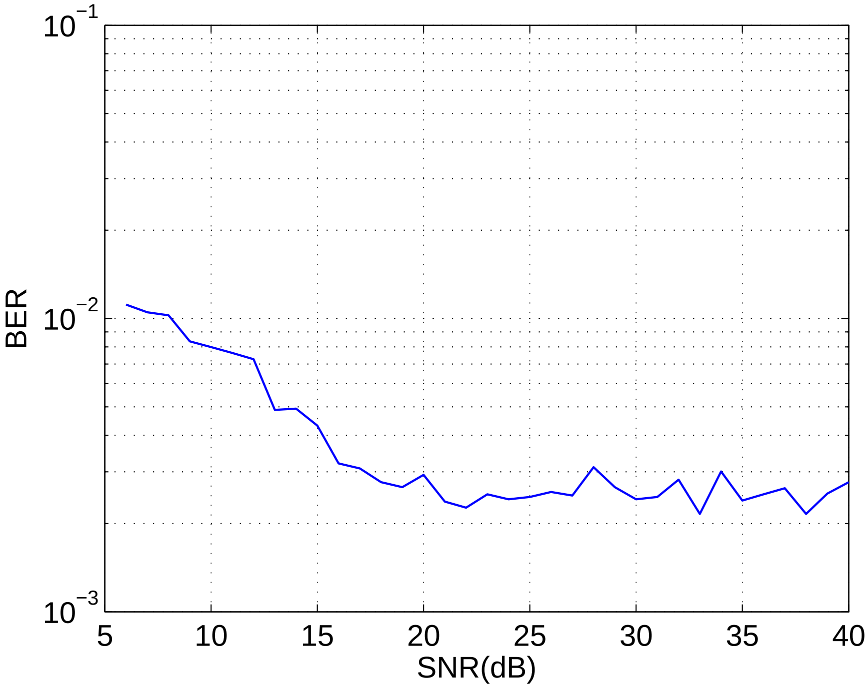

Figure 2.9: Simulation results for the standard Geman and Geman stochastic relaxation algorithm applied to a MRF with correlation parameter $\beta = -3.0$, that has passed through the 2D ISI channel with 2×2 averaging mask and AWGN without being interleaved first.

2.2.2 MRF Source and Unknown Markov Parameters at the Receiver

If the MRF detector must estimate the Markov model parameters, there will be some estimation error between the actual and estimated parameters. This leads to the question: how accurate must the model parameters be in order to achieve performance gains similar to those seen when the parameters are known exactly?

To answer this question, we did a number of simulations using the equiprobable MRFs of Fig. 2.2(b) and (c), in which the assumed MRF parameter β did not match the actual parameter. These simulation results are shown in Figs. 2.10 and 2.11. In Fig. 2.10 the source image has $\beta = -1.5$. At high SNR, there is a mismatch penalty of about 0.2 or 0.3

dB when the receiver assumes that β is one of the values $(-0.5, -0.75, -3.0)$, but this still leads to a gain of about 0.2 dB over the ISI-only case. Only when β is assumed to be -4.5 does the concatenated system perform worse than the ISI detector alone. Interestingly, at low SNR, the assumed values of -3.0 and -4.5 give almost identical results to the correct value of -1.5. The concatenated system thus appears to be quite robust to receiver parameter mismatch, at both high and low SNRs.

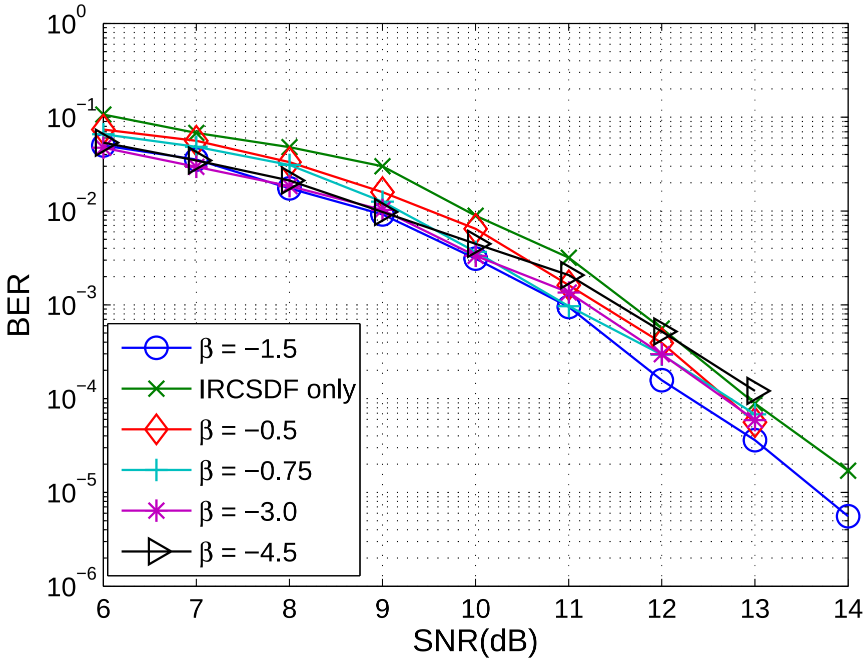

Figure 2.10: Simulation results for the concatenated system on the 2D ISI channel with 2×2 averaging mask, for the $\beta = -1.5$ binary MRF of Fig. 2.2(b) with receiver parameter mismatch.

The results shown in Fig. 2.11, where the source MRF has $\beta = -3.0$, suggest that robustness to parameter mismatch increases as the source MRF becomes more correlated. At high SNR, assumed values of β in a range between -1.5 and -10.0 give gains of more than 1 dB compared to ISI-only detection; assumed values of -4.5 and -6.0 perform as well as the correct value of $\beta = -3.0$.

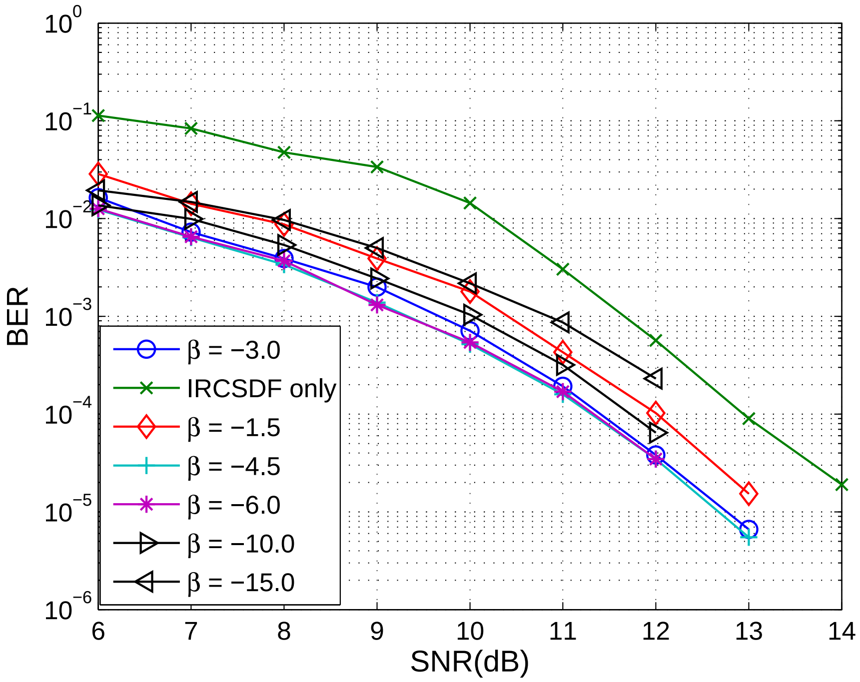

Figure 2.11: Simulation results for the concatenated system on the 2D ISI channel with 2×2 averaging mask, for the $\beta = -3.0$ binary MRF of Fig. 2.2(c) with receiver parameter mismatch.

2.2.3 Natural Image Sources

We also tested the performance of our concatenated MRF-ISI detector on the some natural binary images. Without doing any model estimation, we simply used our first order MRF model with several guessed values of β to model these images.

First we consider two 64×64 natural binary images “chair” and “man” shown in Fig. 2.12. In these images, the numbers of 0s and 1s are nearly equal, so we used the equiprobable version of the MRF-ISI system.

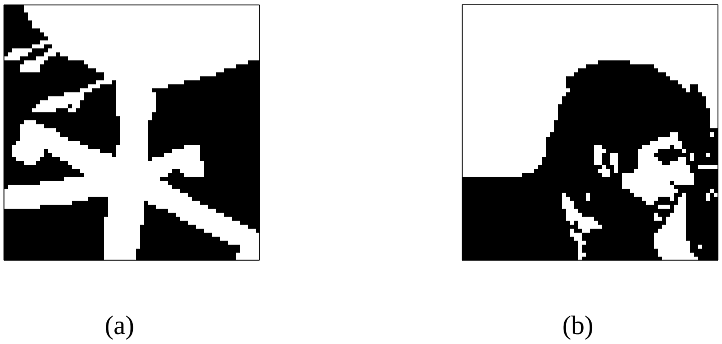
(a) (b)

Figure 2.12: Two 64×64 natural binary images: (a) chair, and (b) man.

The guessed β value used here are -1.5, -3.0, -4.5, and -6.0. The simulation results for the chair and man images appear in Figs. 2.13 and 2.14. For these natural images at high SNR, the concatenated detector achieves SNR savings of between 1 and 2 dB compared to the ISI-only detector, for a wide choice of β values at the receiver.

Then we tested the performance of our concatenated MRF-ISI detector on the three 256×256 natural binary images "Lena", "text" and "rice" shown in Fig. 2.15, and on a 512×512 binary version of "Lena" we called "Lena512." The probabilities p_0 of the three 256×256 images are 0.6951, 0.9411 and 0.7139 respectively, and their variances after the interleaver are 0.2094, 0.0548 and 0.0574 respectively. The quantization threshold for the "Lena512" image was adjusted so that its value of p_0 was 0.6929, very close to that for the 256×256 "Lena." The non-equiprobable version of the MRF-ISI system was used to process these natural binary images.

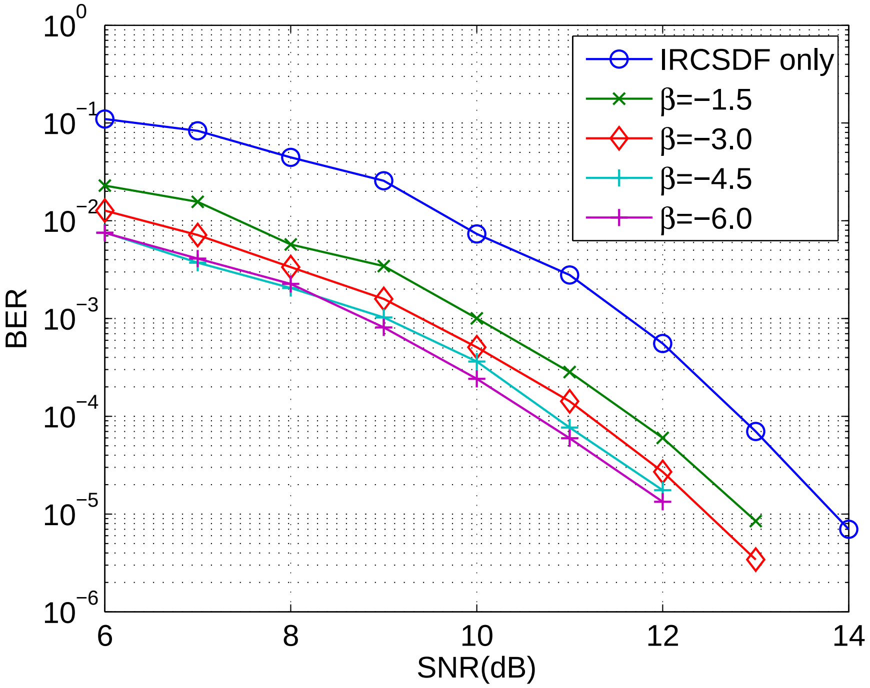

Figure 2.13: Simulation results for the concatenated system on the 2D ISI channel with 2×2 averaging mask, on the natural binary image "chair" of Fig. 2.12, for various values of MRF parameter β.

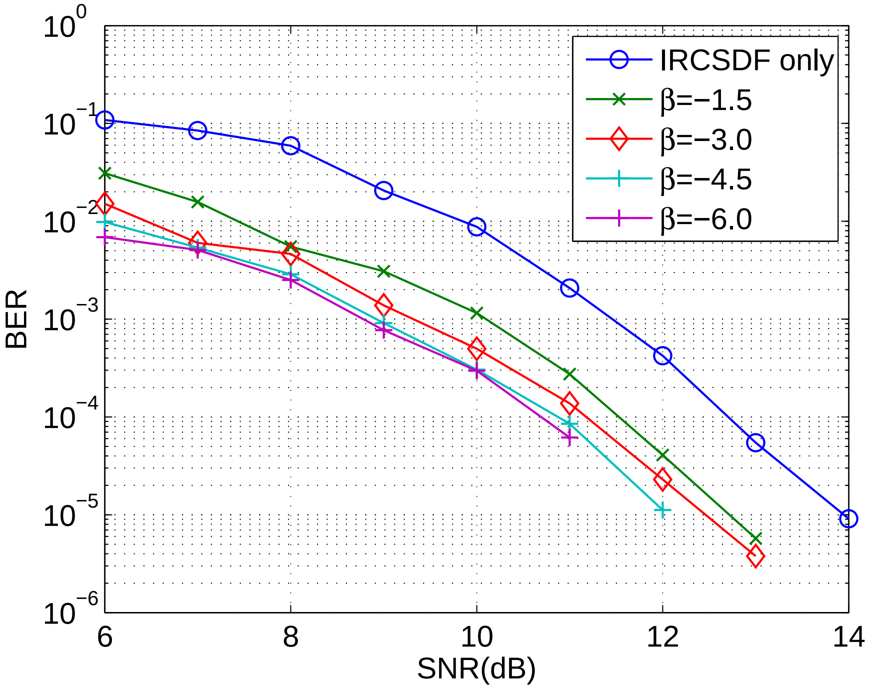

Figure 2.14: Simulation results for the concatenated system on the 2D ISI channel with 2×2 averaging mask, on the natural binary image “man” of Fig. 2.12, for various values of MRF parameter β.

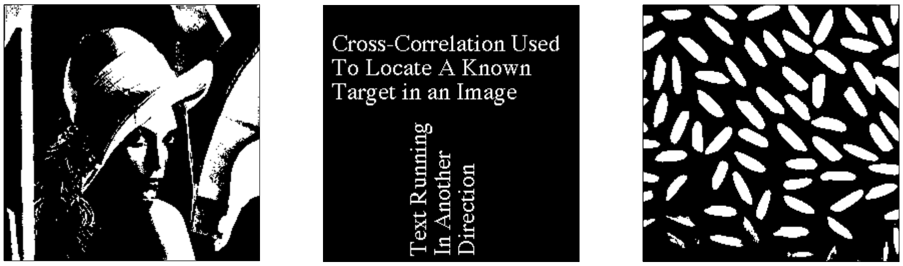

(a) (b) (c)

Figure 2.15: Three 256×256 natural binary images: (a) Lena, (b) text and (c) rice.

Without doing any model estimation, we simply used our first order MRF model with several guessed values of β between -1.5 to -15.0 to model these three images, and chose one β which had the best performance for each image. For these images, the performance degraded by no more than 0.1 dB for βs within $\pm 30\%$ of the chosen value. In particular, we chose $\beta = -4.5$ for "Lena" and "text", $\beta = -10.0$ for "rice", and $\beta = -1.5$ for "Lena512." The simulation results appear in Fig. 2.16, where at BER 10^{-4} "Lena" has a SNR gain of about 1.5 dB compared to the ISI-only detector, "Lena512" has a gain of about 0.2 dB, "text" has a gain of 0.7 dB, and "rice" has a gain of 2 dB. The gain for "Lena512" was smaller than for "Lena", probably because the greater detail of the larger image reduced the correlation after quantization. We also noticed that "text" and "rice" have lower SNR than "Lena"; this is because their variances are smaller than that of "Lena." For these natural images at high SNR, the concatenated detector achieves SNR savings of between 0.2 and 2 dB compared to the ISI-only detector, thereby demonstrating that a simple first-order MRF model is very useful in reducing 2D ISI in natural binary images.

In order to examine the performance of our MRF-ISI detector on compressed gray-level images, we computed a one-level wavelet transform of the 256×256 8-bit Lena image, and then quantized to 8 bits (sign and magnitude format). The standard 9/7 Daubechies bi-orthogonal wavelet transform [48] was used. The quantized version of the bit 7 bit-plane (i.e., the MSB, which was the sign bit) is shown in Fig. 2.17. Then we use the 128×128 low pass subband to run the simulation. When the bit 7 bit-plane was used as the source image, the probability p_0 of this images was 0.6150 and the variance after the iterleaver

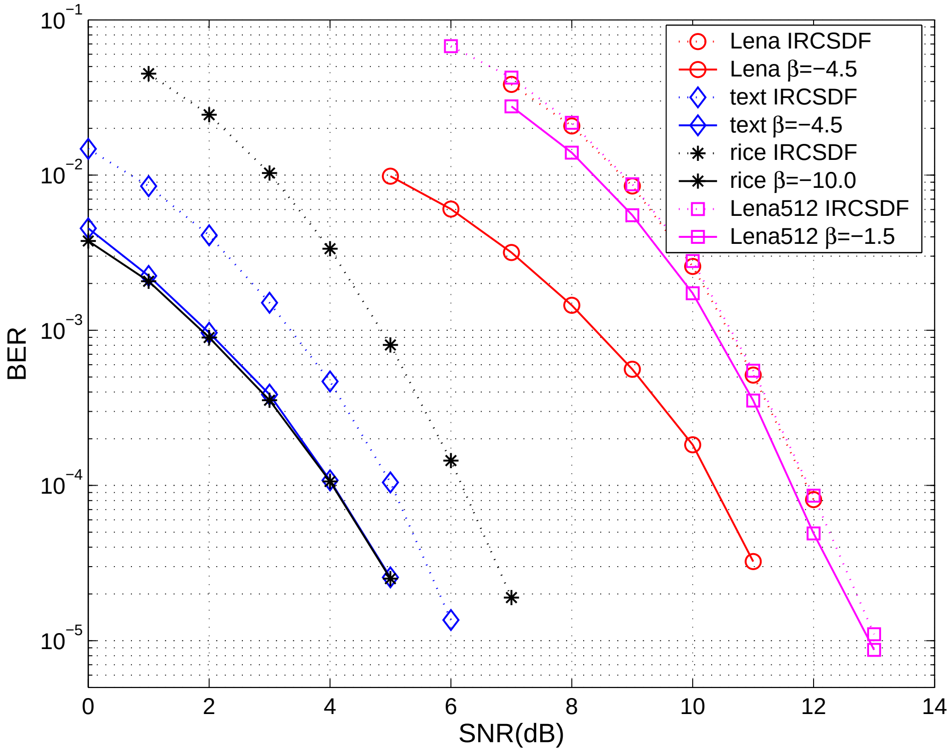

Figure 2.16: Simulation results for the concatenated system on the 2D ISI channel with 2×2 averaging mask, on the natural binary images of Fig. 2.15 with best chosen values of MRF parameter β.

Figure 2.17: MSB of wavelet transformed Lena image

was 0.2320. So we used the non-equiprobable version of the MRF-ISI system to run the simulation. The simulation results appear in Fig. 2.18, where the MRF-ISI detector gave a gain of 0.2 dB over the ISI-only detector at a BER of 10^{-4}, when the MRF detector assumed that $\beta = -1.5$. When the bit 6 bit-plane was used as the source image, the MRF-ISI detector gave a gain of 1.1 dB, with $\beta = -3.0$. The bit 5 plane gave a gain of 0.2 dB, with $\beta = -1.5$. These experiments demonstrate that the proposed joint MRF-ISI detection scheme can be useful for the higher-order bit-planes of quantized gray-level images.

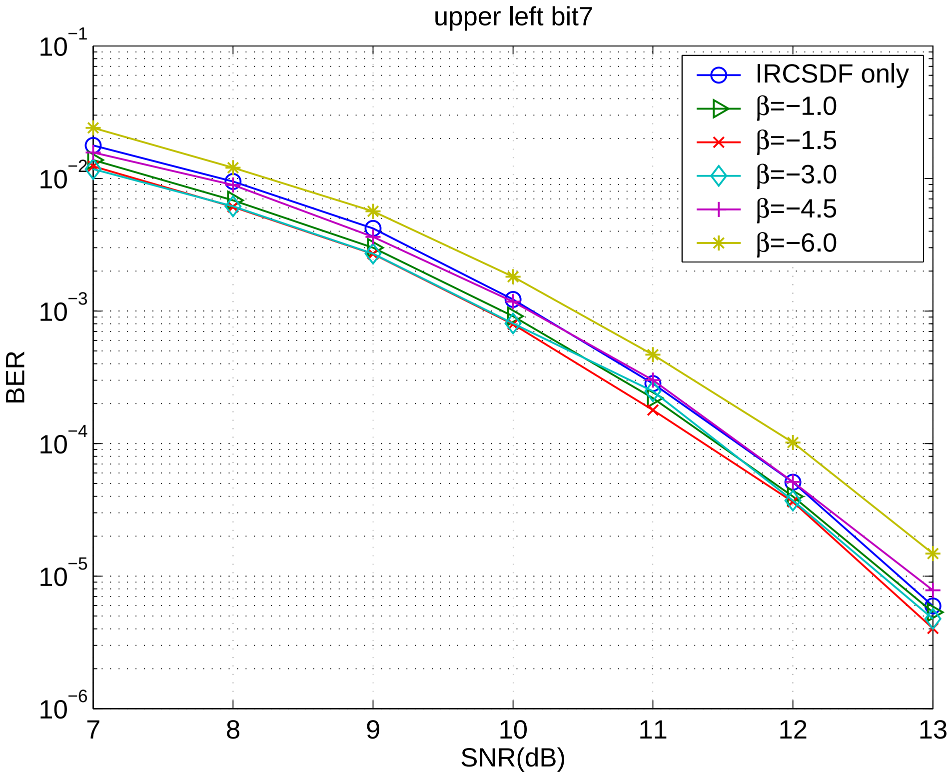

Figure 2.18: Simulation results for bit 7 of low pass subband of Lena image.

Chapter 3

Reduced State BCJR Algorithms for One- and Two-Dimensional Equalization

In this chapter, we present a new truncated state SISO algorithm which is more appropriate for center-weighted masks. The finite-length ISI channel discussed in this chapter is described in section 1.4 and the standard log-MAP version of BCJR is employed to estimate the *a posteriori* probabilities (APPs) of the input symbols.

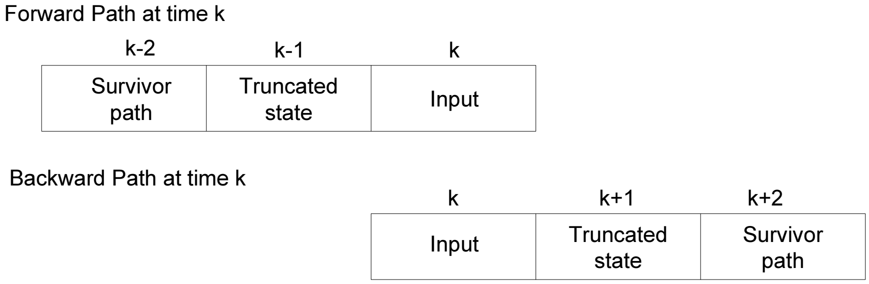

Figure 3.1: Truncated state diagram for the MSM RS-SISO of [40], for 1D mask of length $L = 3$.

3.1 1D Reduced State Algorithms for Center-Weighted Masks

The MSM RS-SISO of [40] defines truncated forward and backward state vectors as in Fig. 3.1, which shows a simple example for $L = 3$. The full-state trellis would have four states, but the truncated-state trellis has only two states. A log-min version of the BCJR algorithm is employed, with different branch metrics $\lambda_k^f(i,j)$ and $\lambda_k^b(i,j)$ for the forward and backward passes; here i and j are state indices of the reduced-state trellis. The branch metrics correspond to the negative log of the $\gamma_k(i,j)$ state transition probabilities. The branch outputs necessary to compute the $\gamma_k(i,j)$s depend on the missing symbols $k-2$ and $k+2$ for the forward and backward passes; these missing symbols are estimated by keeping track of surviving paths (in both the forward and backward directions) into the truncated states. The log-min formulation means that the update equations in both directions are similar to those of the Viterbi algorithm.

We now briefly summarize the update equations from [40]. The forward and backward state metric updates are

$$\delta_{k+1}(j) = \min_{i \in \mathcal{F}(j)} [\delta_k(i) + \lambda_{k+1}^f(i,j)] \tag{3.1}$$

$$\eta_k(i) = \min_{j \in \mathcal{B}(i)} [\eta_{k+1}(j) + \lambda_{k+1}^b(i,j)], \tag{3.2}$$

where $\mathcal{F}(j) = \{i : i \rightarrow j \text{ is an allowed forward transition}\}$ and $\mathcal{B}(i) = \{j : i \leftarrow j \text{ is an allowed backward transition}\}$. The soft output metrics for symbol a_k are computed by minimizing over the sums of the relevant forward and backward state metrics:

$$M^o(a_k = m) = \min_{j \in \mathcal{C}(m)} [\delta_k(j) + \eta_k(j)], \tag{3.3}$$

where $\mathcal{C}(m) = \{j : \text{at time } k+1, \text{state element } a_k = m\}$, and $m \in \{-1, 1\}$. Extrinsic information can be passed either to subsequent iterations of the 1D MSM RS-SISO ("self-iterations"), or to a MSM RS-SISO running in another scanning direction (for 2D ISI detection); the output extrinsic information metric is

$$M_e^o(a_k = m) = M^o(a_k = m) - M^i(a_k = m), \tag{3.4}$$

where $M^i(a_k = m)$ denotes input extrinsic information.

For center weighted masks with small magnitude peripheral taps, the distance differences between surviving path candidates are very small, causing the MSM RS-SISO of [40] to choose incorrect surviving paths and leading to poor detection performance. To solve this problem, we redefine the forward and backward truncated state vectors as in Fig. 3.2, which shows an example for $L = 3$. In these diagrams, the leading bits in the forward and backward directions, which are the input bits in the full-state version, are simply ignored; their contribution to the branch outputs is small due to the small peripheral taps and can therefore be neglected. The indexing of the update equations (3.1)-(3.3) is adjusted to account for the offset between the estimated input bit in the forward and backward directions

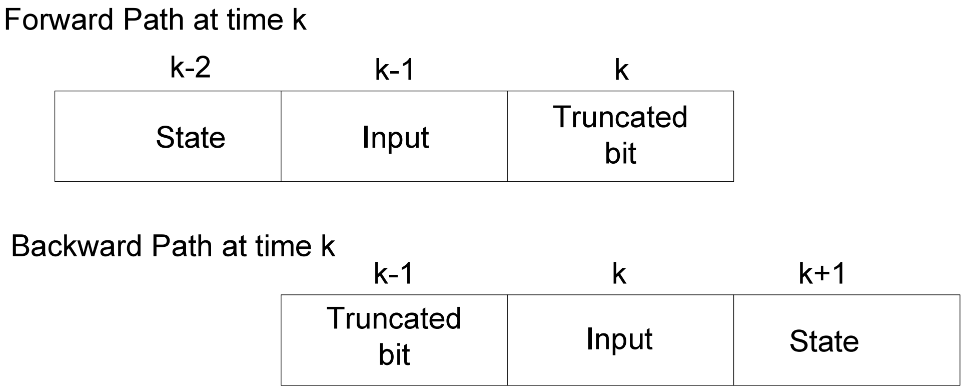

Figure 3.2: Truncated state diagram for the new MSM RS-SISO algorithm for center-weighted masks of length $L = 3$.

in the new state vectors; no such offset is present in the original state vector definitions shown in Fig. 3.1. Because the truncated bits are ignored, there is no need to estimate them using surviving paths.

For the 1D mask of length $L = 3$, the fully connected trellis has four states with two branches out of each state. By comparison, both the algorithm of [40] (due to Chen and Chugg) and our proposed algorithm have two states with two branches out of each state, which is equivalent in complexity to the M-BCJR algorithm with $M = 2$.

3.1.1 Simulation Results

We consider the 1D channel $[\alpha\ 1\ \alpha]$ with $\alpha = 0.1, 0.2, 0.8$ and 1.0. We compare the performance of our proposed algorithm with that of the M-BCJR algorithm [41] for $M = 2$ and Chugg's algorithm [40]. The union upper bound on the performance of the ML equalizer is also shown for comparison; this bound is tight at high SNR. The results for $\alpha = 0.1, 0.2$ are shown in Fig. 3.3; this figure also shows the results of simple hard decision demodulation (without equalization) for these channels. Fig. 3.4 depicts similar results for $\alpha = 0.8, 1.0$. With reference to the channel model (1.18), the SNR in all simulations reported in this dissertation is

$$\text{SNR} = 10\log_{10}\left(\text{var}\left[\mathbf{a} * \mathbf{h}\right]/\sigma_w^2\right), \tag{3.5}$$

where $*$ denotes 1- or 2-D convolution, and σ_w^2 is the variance of the elements of the noise vector $\mathbf{w}$ in (1.18).

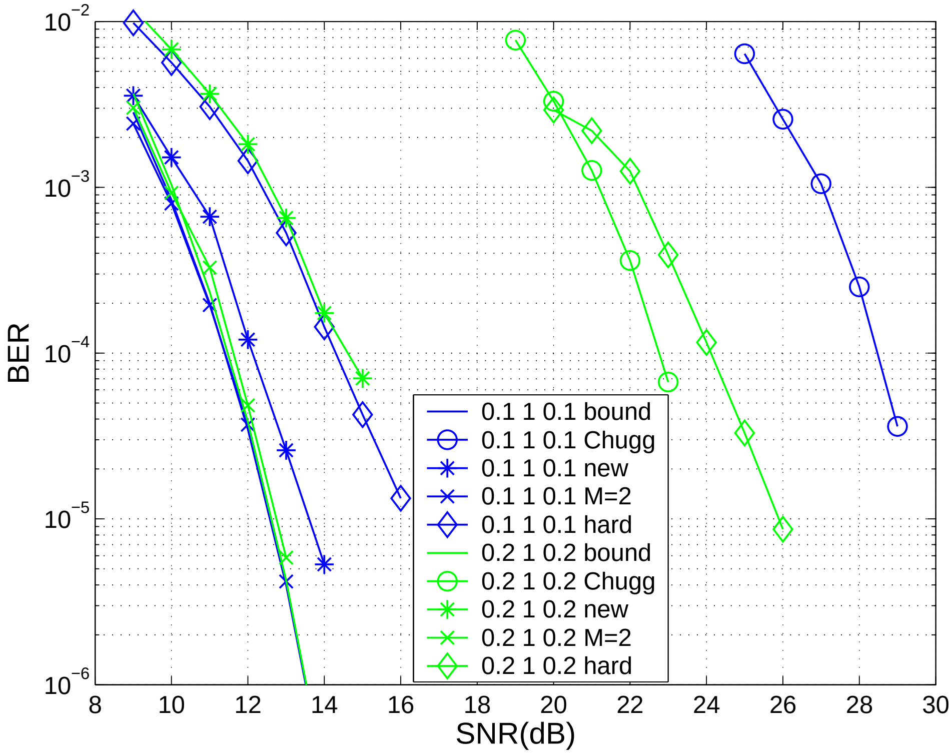

Figure 3.3: 1D simulation results for masks $[0.1\ 1\ 0.1]$ and $[0.2\ 1\ 0.2]$.

When $\alpha = 0.1$ or 0.2, M-BCJR with $M = 2$ gives the best performance, which is very close to the ML bound. For $\alpha = 0.1$, our proposed algorithm is about 0.7 dB away and Chugg's algorithm is about 17 dB away from the ML bound, while the hard-decision curve is about 2.9 dB from the bound. For $\alpha = 0.2$, our proposed algorithm is about 3 dB away and Chugg's algorithm is about 11 dB away from the ML bound, while the hard-decision curve is about 12.5 dB from the bound. When $\alpha = 0.8$ or 1.0, M-BCJR with $M = 2$ again gives the best performance, which is 0.6 dB away from the ML bound. For $\alpha = 0.8$ ($\alpha = 1.0$), Chugg's algorithm is 0.8 dB (0.9 dB) away from the ML bound, whereas our proposed algorithm completely fails in both cases. All comparisons are done at a BER of 10^{-4}.

Since our proposed algorithm truncates one state bit, it is expected to perform well when the contribution of the truncated mask element is small. In the current example, this happens when the value of α is small.

3.2 2D Reduced State Algorithms for Center-Weighted Masks

Fig. 3.5 shows the truncated state and input block for the row-trellis of IRCSDF algorithm of [3], for a 3×3 ISI mask. This modified IRCSDF algorithm uses MSM RS-SISOs (like those in [40]) in row and column directions; the SISOs iteratively exchange extrinsic information until convergence occurs. A similar input block, rotated right by 90 degrees, defines the column trellis.

Trellis generation for the 3×3 mask on the mth image row is initiated by placing the

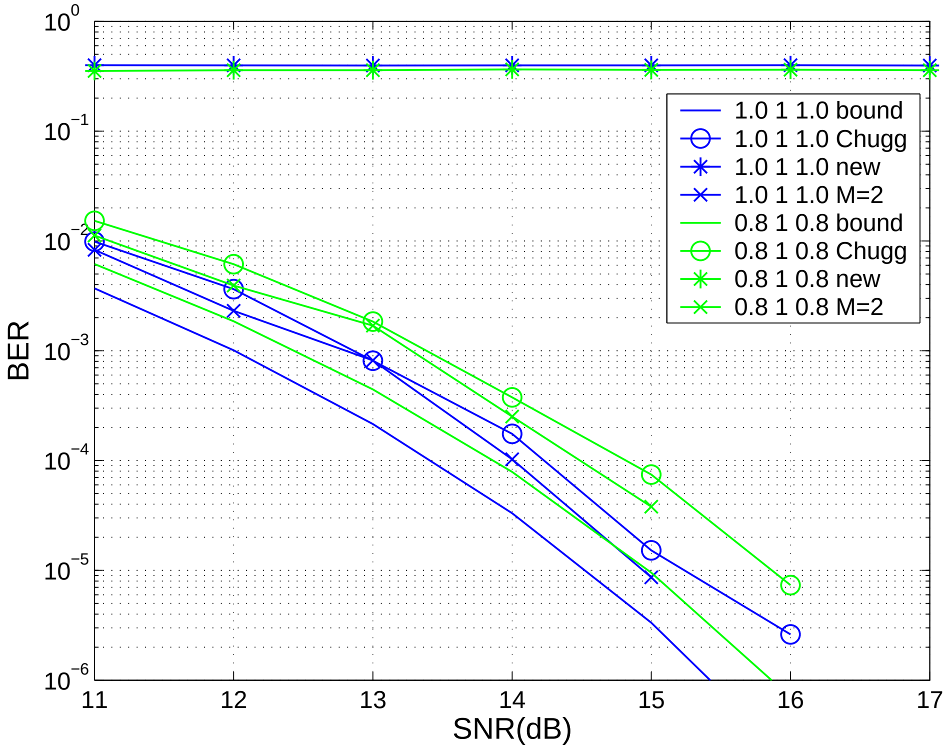

Figure 3.4: 1D simulation results for masks $[0.8\ 1\ 0.8]$ and $[1\ 1\ 1]$.

input marked (m, n) in Fig. 3.5 (the uppermost of the three inputs) at the left end of the row, where the initial values of the six state pixels (which include the three truncated state pixels on the left) are -1 due to the boundary conditions, and the vector of three input pixels can take eight different values. The entire state/input block is then shifted right to pick up the next three input pixels, and the previous three input pixels become the middle three state pixels. The full-state trellis therefore has 64 states with 8 branches out of each state. The Chugg-style truncation scheme shown in Fig. 3.5 has eight states with eight branches out of each state; the deleted state pixels are estimated by surviving paths in the forward and backward passes of the MSM RS-SISO algorithm. At each position (m, n),

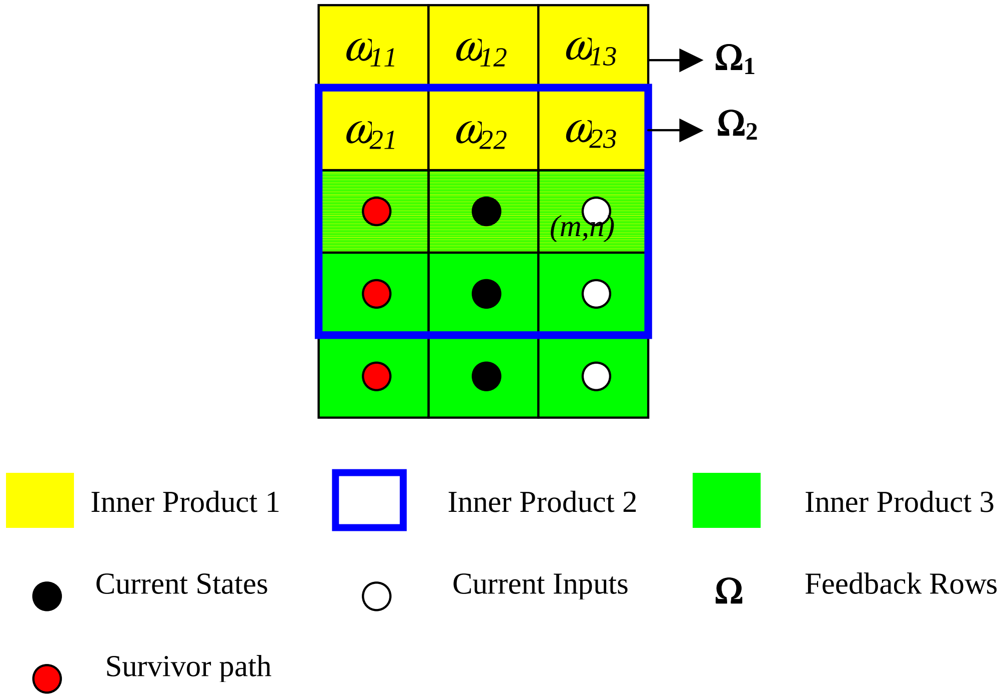

Figure 3.5: 2D truncated state diagram for the forward row pass of the IRCSDF algorithm of [3] on a 3×3 ISI channel.

the trellis branch output vector consists of three 3×3 inner products between the inverted mask and the pixel values defined by the trellis; the upper inner product feedback from two previously processed rows, the middle uses one feedback row, and the lower uses received pixels only. The branch metric is the squared Euclidean distance between the branch output and the received pixel vector $[r(m,n), r(m+1,n), r(m+2,n)]$.

Fig. 3.6 shows the truncated state diagram for the row-trellis of an IRCSDF algorithm employing the new MSM-RS-SISO of section 3.1. The new MSM-RS-SISO algorithm is used in row and column directions. This truncation scheme works well for center weighted masks in which the relative magnitude of the edge coefficients on each row (column) are much smaller than those of the center coefficient. As with the truncation scheme shown

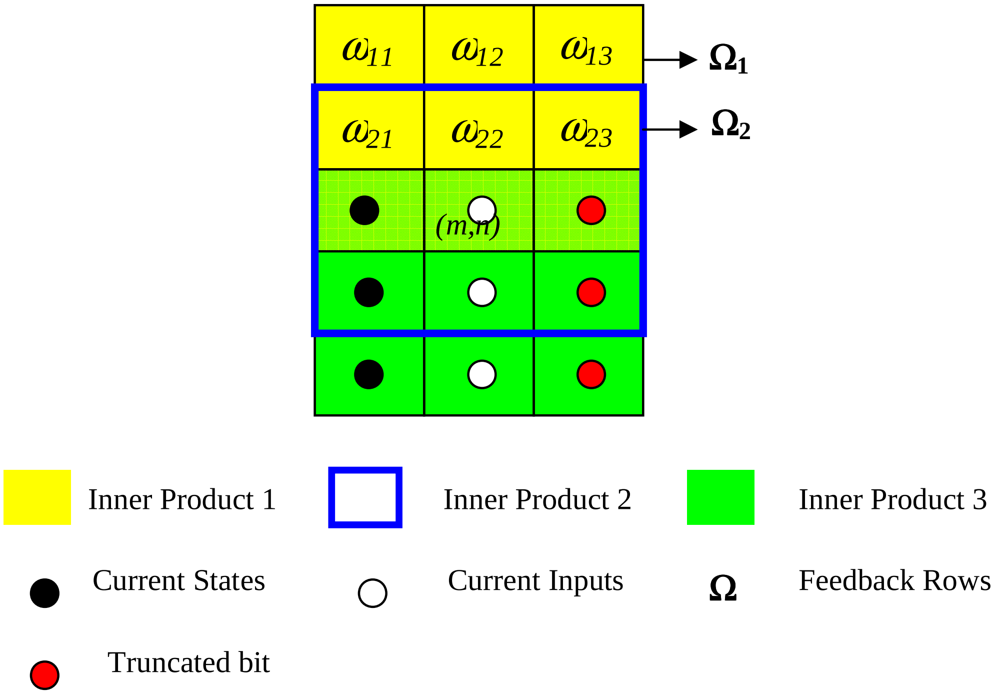

Figure 3.6: Proposed new truncated state diagram for the forward row pass of the IRCSDF algorithm on a 3×3 ISI channel.

in Fig. 3.5, the truncated trellis has 8 states and 8 branches per state. Thus, both truncated IRCSDF algorithms are equivalent in complexity to an IRCSDF algorithm which employs the M-BCJR algorithm with $M = 8$ in its row and column detectors; performance comparisons between these three algorithms are made in the following section.

3.2.1 Simulation Results

We consider the 3×3 channel mask the "α channel",

$$\begin{pmatrix} 0 & \alpha & 0 \\ \alpha & 1 & \alpha \\ 0 & \alpha & 0 \end{pmatrix}. \tag{3.6}$$

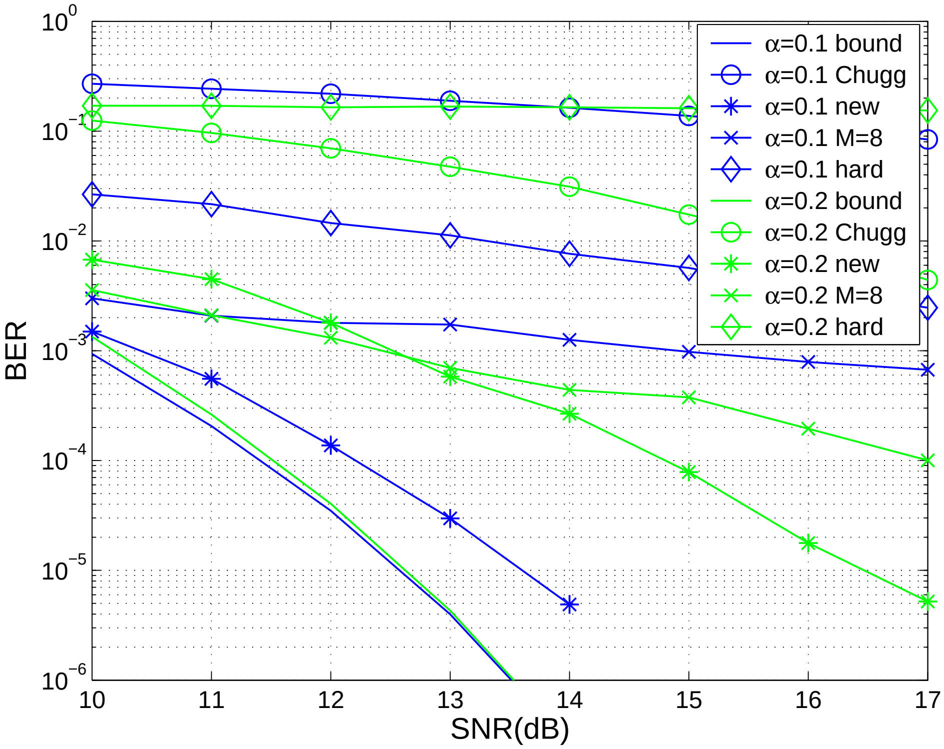

Figure 3.7: 2D-ISI simulation results for 3×3 center-weighted masks with $\alpha = 0.1, 0.2$.

We compare the performance of our proposed algorithm (corresponding to Fig. 3.6) with that of $M = 8$ M-BCJR [41] and Chugg's algorithm (corresponding to Fig. 3.5). The ML bound is also shown for comparison. The results for $\alpha = 0.1, 0.2$ are shown in Fig. 3.7; this figure also shows the results of simple hard decision demodulation for these channels. Fig. 3.8 depicts similar results for "Channel B" and the averaging mask. The 3×3 "Channel B" mask [6] is

$$\begin{pmatrix} 0.0993 & 0.352 & 0.0993 \\ 0.352 & 1 & 0.352 \\ 0.0993 & 0.352 & 0.0993 \end{pmatrix}. \tag{3.7}$$

The 3×3 averaging mask has all elements equal to 1.0. Six iterations of the IRCSDF algorithm were used for all simulations shown in Fig. 3.7 and Fig. 3.8, with the exception of the hard-decision simulations.

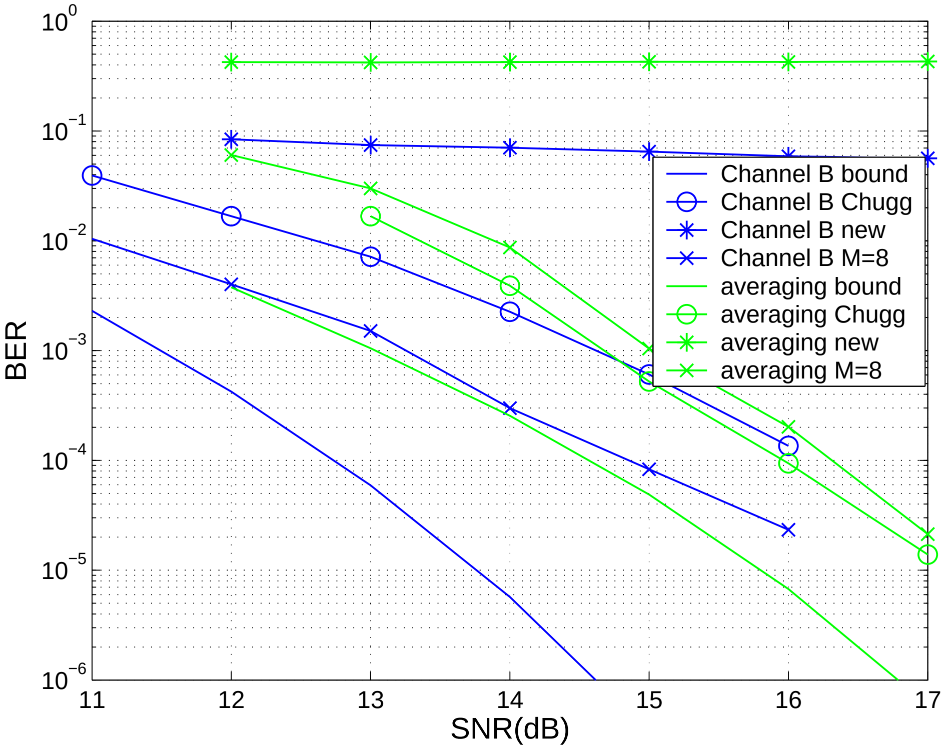

Figure 3.8: 2D-ISI simulation results for 3×3 masks, the “Channel B” mask and the averaging mask.

When $\alpha = 0.1$, the performance of the new algorithm (0.7 dB away from ML bound) is better than that of the $M = 8$ M-BCJR algorithm (more than 6 dB away from ML bound). When $\alpha = 0.2$, the performance of the new algorithm (3 dB away from ML bound) is again better than that of $M = 8$ M-BCJR (5.5 dB away from ML bound). Chugg’s algorithm fails for both $\alpha = 0.1, 0.2$, as does hard-decision demodulation. For Channel B, the performance of $M = 8$ M-BCJR (2 dB away from ML bound) is better than that of Chugg’s algorithm (3.4 dB away from ML bound). For the averaging mask, the performance of Chugg’s algorithm (1.3 dB away from ML bound) is better than that of $M = 8$ M-BCJR (1.8 dB away from ML bound). Our proposed algorithm fails for Channel B and the averaging mask. All comparisons are done at a BER of 10^{-4}.

3.3 2D ISI M-BCJR Algorithm Comparison

In the M-BCJR algorithm we used, the surviving states were picked only from the forward direction. In [49], the forward direction selects the M states with the highest forward state probabilities $\alpha(m)$ and retains only those states and their connecting branches. The backward pass employs the same strategy, using the backward state probabilities $\beta(m)$ to independently choose the backward-pass active states. We apply this method in our 2D ISI problem. Instead of weighting the extrinsic information in every iteration, [49] uses a parameter γ, in the range $[0, 1]$, to perform *output saturation*. For each time epoch k, the ratio between the lowest extrinsic information and the largest one must be at least equal to γ. We tested several values of γ with the 2D averaging mask; the results are shown in Fig. 3.9, where the curve labelled “averaging M=8” is the one using our old method, which is identical with the “averaging M=8” curve in Fig. 3.8. From Fig. 3.9 we can see, the new method works better at low SNR but performs almost the same as the old method at high SNR.

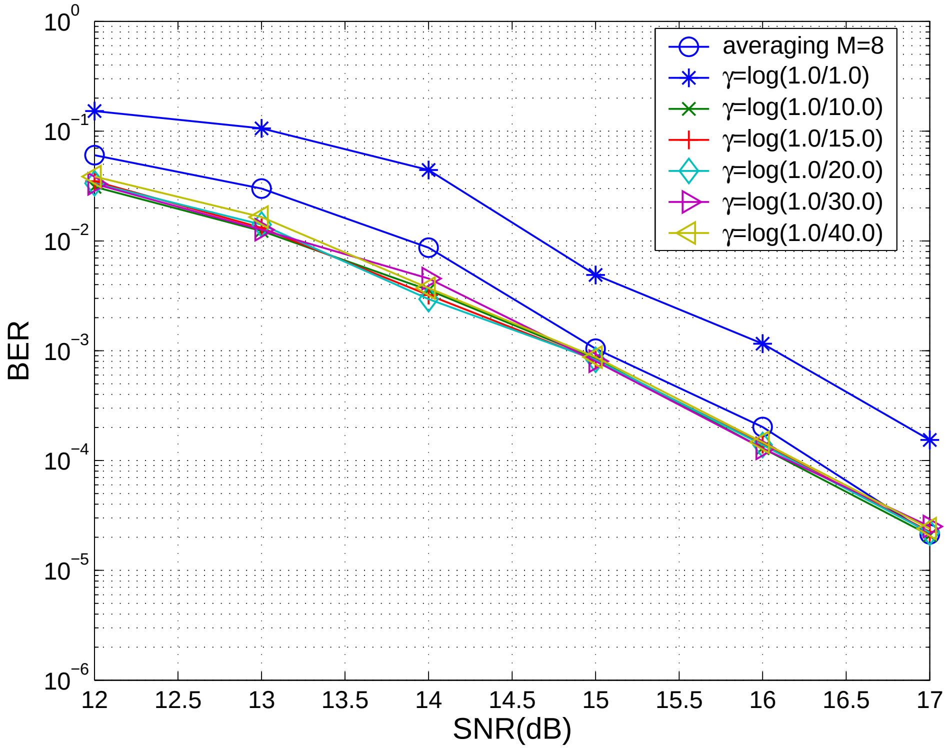

Figure 3.9: 2D-ISI M-BCJR simulation results for the averaging mask.

Chapter 4

4-ary Modulation for 2D-ISI Channels

For 2D storage systems, the storage capacity can be increased by using more than two levels. In this chapter, we will compute equivalent masks for 4-ary and binary modulation for Gaussian and Sinc square point spread functions (PSFs). For 4-ary and binary, at the same areal density, when we chose different parameters, for some cases, 4-ary modulation can give better performance than binary modulation.

4.1 System Presentation

The basic system architecture of the parallel optical binary detection system is shown in Fig 4.1. This figure is copied from [22]. L1 and L2 are Fourier transform lenses, XTAL is a photo refractive crystal, and REF represents the reference beam. SLM is a spatial light modulator. CCD is a charge-coupled device. During recording a binary amplitude SLM transmits the 2D binary data into the optical recording system. The overall noncoherent system PSF is defined as:

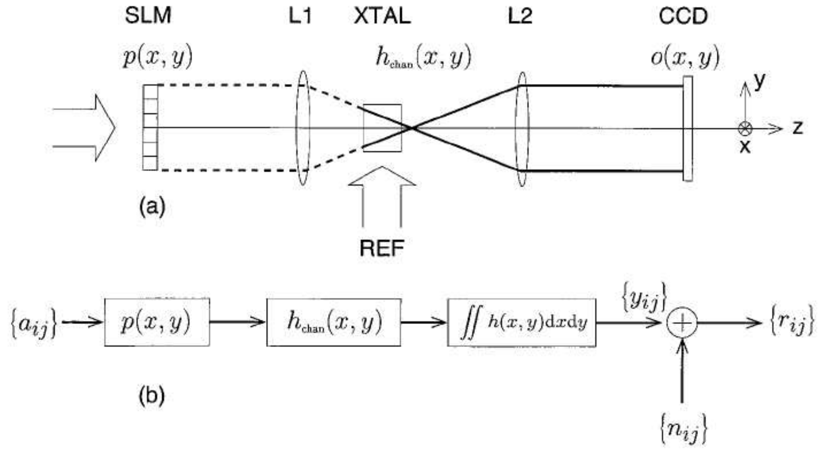

Figure 4.1: Parallel optical binary detection system: (a)system architecture and (b)system model.

$$h(x, y) = p(x, y) * h_{chan}(x, y) \tag{4.1}$$

where $*$ denotes 2D convolution.

The discrete PSF can be defined as:

$$h_{kl} = \int_{y_k^-}^{y_k^+} \int_{x_l^-}^{x_l^+} h(x, y) dx dy \tag{4.2}$$

where $x_l^{\pm} = lD \pm \gamma/2$, $y_k^{\pm} = kD \pm \gamma/2$, D is the SLM pixel pitch, and γ is the CCD pixel size. For simplicity, we set $D = 1$ and $\gamma = 1$.

From 4-ary to binary, to keep the same areal density, Fig. 4.2 shows that we can change both the CCD pixel size γ and SLM pixel pitch D from 1 to $1/\sqrt{2}$.

If we use the same equation to compute SNR for binary and 4-ary sources, the SNR for 4-ary would be “SNR per symbol”. Since $E_s = 2E_b$, “SNR per bit” equals “SNR per symbol”$-$ 3dB.

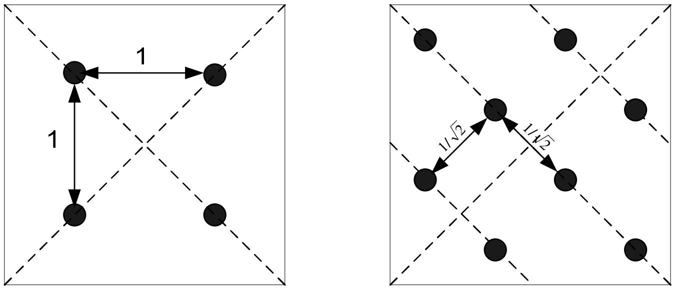

(a) 4-ary (b) binary

Figure 4.2: Example of symbol positions for (a)4-ary and (b)binary in same area.

4.1.1 Gaussian PSF

We call the PSF “Gaussian PSF” if the computed values of the discrete PSF are based on the use of a radially symmetric Gaussian blur spot with width σ_b:

$$h(k,l) = \int_{(k-1/2)/\delta}^{(k+1/2)/\delta} \int_{(l-1/2)/\delta}^{(l+1/2)/\delta} \exp[-(x^2+y^2)/2\sigma_b^2]dxdy, \tag{4.3}$$

where $\delta = 1$ for 4-ary and $\delta = \sqrt{2}$ for binary.

The Sparrow criterion specifies that the noncoherent intensity superposition of two neighboring pixels yields an intensity profile that has a point of inflection at the spatial position half-way between the two pixels. For a Gaussian blur function, the resolution limit (Sparrow limit) is achieved for $\sigma_b = 0.5$; the corresponding discrete PSF is

$$\begin{bmatrix} 0.000280588 & 0.00373363 & 0.00872232 & 0.00373363 & 0.000280588 \\ 0.00373363 & 0.0496814 & 0.116063 & 0.0496814 & 0.00373363 \\ 0.00872232 & 0.116063 & 0.271141 & 0.116063 & 0.00872232 \\ 0.00373363 & 0.0496814 & 0.116063 & 0.0496814 & 0.00373363 \\ 0.000280588 & 0.00373363 & 0.00872232 & 0.00373363 & 0.000280588 \end{bmatrix}. \tag{4.4}$$

With the same areal density, the 4-ary discrete PSF is

$$\begin{bmatrix} 1.82145^{-6} & 0.000212 & 0.00092 & 0.000212 & 1.82145^{-6} \\ 0.000212 & 0.024745 & 0.107391 & 0.024745 & 0.000212 \\ 0.000921 & 0.107391 & 0.466065 & 0.107391 & 0.0009213 \\ 0.000212 & 0.024745 & 0.107391 & 0.024745 & 0.000212 \\ 1.82145^{-6} & 0.000212 & 0.00092 & 0.000212 & 1.82145^{-6} \end{bmatrix}. \tag{4.5}$$

The ML bounds for these two PSFs are shown in Fig. 4.3. In this case, the binary modulation performs about 1.2dB better than the 4-ary modulation.

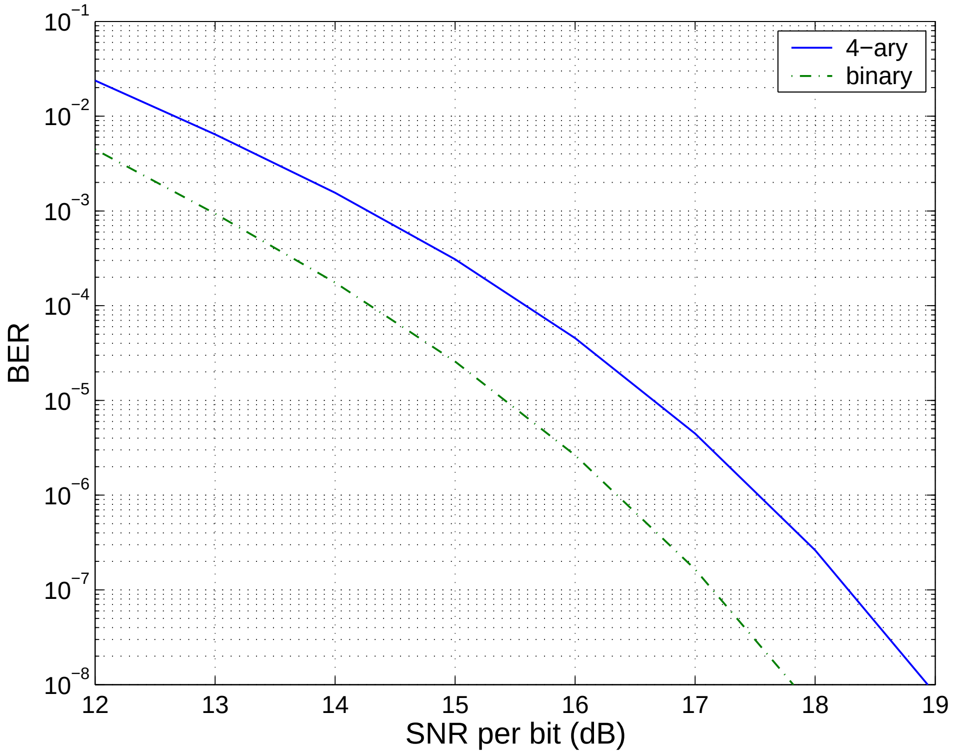

Figure 4.3: ML bound for Gaussian PSF with $\sigma_b = 0.5$

The binary and 4-ary PSFs for $\sigma_b = 0.6$ are:

Binary:

$$\begin{bmatrix} 0.0013648 & 0.00884065 & 0.0164148 & 0.00884065 & 0.0013648 \\ 0.00884065 & 0.0572663 & 0.106329 & 0.0572663 & 0.00884065 \\ 0.0164148 & 0.106329 & 0.197426 & 0.106329 & 0.0164148 \\ 0.00884065 & 0.0572663 & 0.106329 & 0.0572663 & 0.00884065 \\ 0.0013648 & 0.00884065 & 0.0164148 & 0.00884065 & 0.0013648 \end{bmatrix}, \tag{4.6}$$

4-ary:

$$\begin{bmatrix} 0.0000383706 & 0.00121488 & 0.00368791 & 0.00121488 & 0.0000383706 \\ 0.00121488 & 0.0384649 & 0.116765 & 0.0384649 & 0.00121488 \\ 0.00368791 & 0.116765 & 0.354455 & 0.116765 & 0.00368791 \\ 0.00121488 & 0.0384649 & 0.116765 & 0.0384649 & 0.00121488 \\ 0.0000383706 & 0.00121488 & 0.00368791 & 0.00121488 & 0.0000383706 \end{bmatrix}. \tag{4.7}$$

The ML bounds for these two PSFs are shown in Fig. 4.4, where the binary ML bound is computed using the 5×5 PSF of (4.6). The 4-ary ML bounds computed using the center 3×3 PSF of (4.7) and the full 5×5 PSF of (4.7) are very close. The BERs for binary and 4-ary modulation intersect at an SNR around 16.5dB. At BER of 10^{-8}, the SNR savings for 4-ary modulation is about 0.6dB.

The binary and 4-ary PSFs for $\sigma_b = 0.707107 = 1/\sqrt{2}$ are:

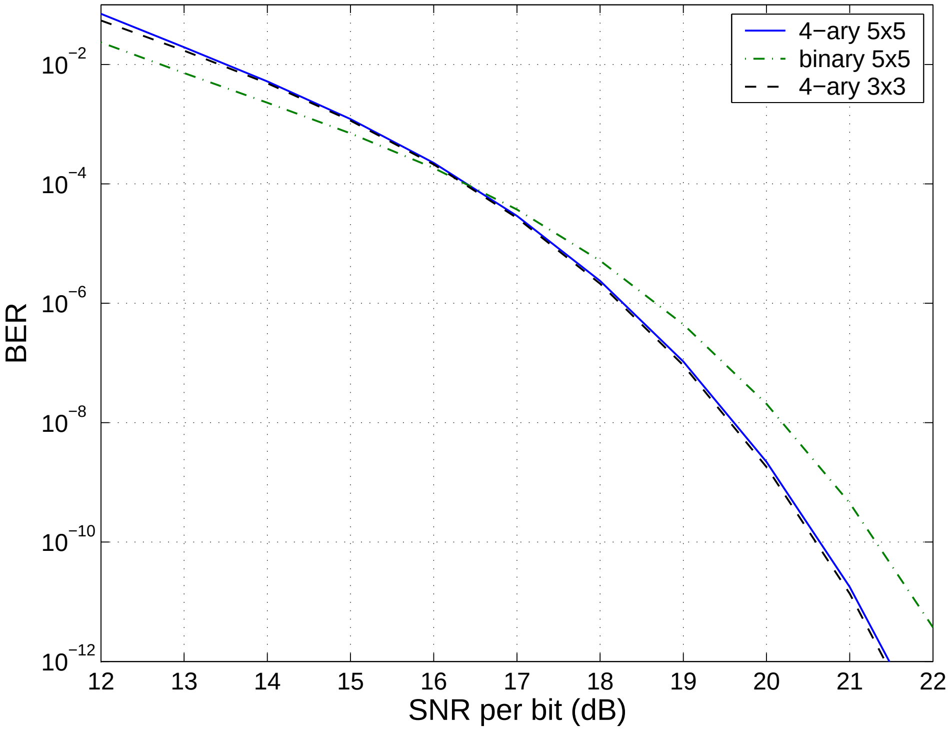

Figure 4.4: ML bound for Gaussian PSF with $\sigma_b = 0.6$

Binary:

$$\begin{bmatrix} 0.0000358 & 0.000363 & 0.00145 & 0.00229 & 0.00145 & 0.000363 & 0.0000358 \\ 0.000363 & 0.00368 & 0.0147 & 0.0232 & 0.0147 & 0.00368 & 0.000363 \\ 0.00145 & 0.0147 & 0.0585 & 0.0927 & 0.0585 & 0.0147 & 0.00145 \\ 0.00229 & 0.0232 & 0.0927 & 0.147 & 0.0927 & 0.0232 & 0.00229 \\ 0.00145 & 0.0147 & 0.0585 & 0.0927 & 0.0585 & 0.0147 & 0.00145 \\ 0.000363 & 0.00368 & 0.0147 & 0.0232 & 0.0147 & 0.00368 & 0.000363 \\ 0.0000358 & 0.000363 & 0.00145 & 0.00229 & 0.00145 & 0.000363 & 0.0000358 \end{bmatrix}, \quad (4.8)$$

4-ary:

$$\begin{bmatrix} 0.000280588 & 0.00373363 & 0.00872232 & 0.00373363 & 0.000280588 \\ 0.00373363 & 0.0496814 & 0.116063 & 0.0496814 & 0.00373363 \\ 0.00872232 & 0.116063 & 0.271141 & 0.116063 & 0.00872232 \\ 0.00373363 & 0.0496814 & 0.116063 & 0.0496814 & 0.00373363 \\ 0.000280588 & 0.00373363 & 0.00872232 & 0.00373363 & 0.000280588 \end{bmatrix}. \tag{4.9}$$

The ML bounds for these two PSFs are shown in Fig. 4.5. where the 4-ary ML bound is computed using the 5×5 PSF. The binary ML bounds for this case suggest that we should use the 7×7 PSF, although the 5×5 PSF from the center of (4.8) gives results that are very close. At BER of 10^{-8}, the SNR savings for 4-ary modulation is about 2dB.

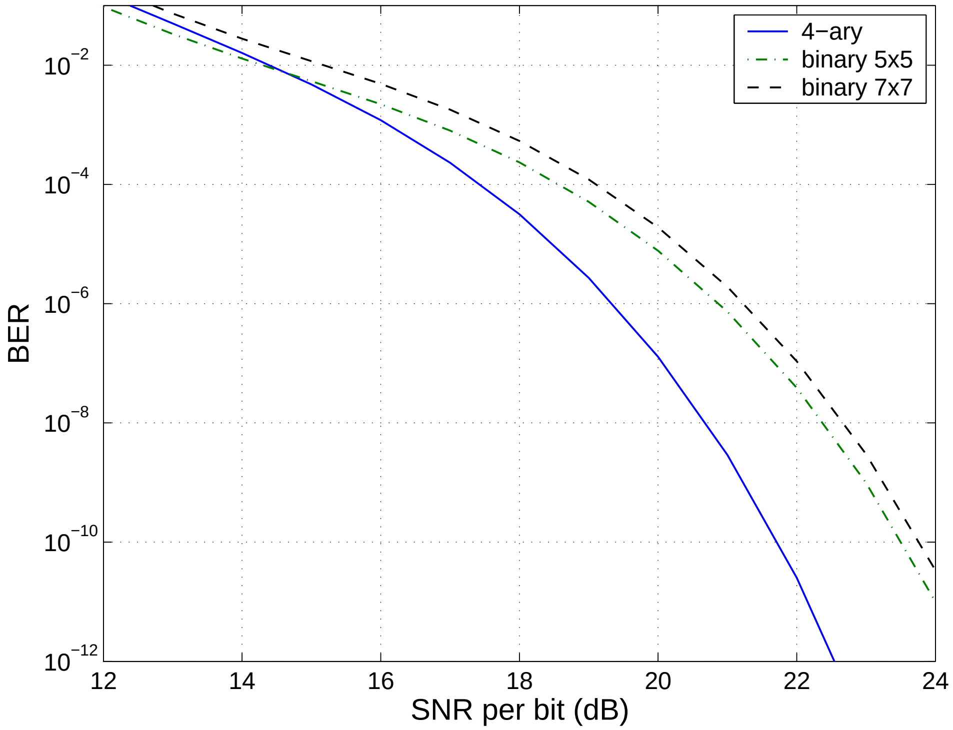

Figure 4.5: ML bound for Gaussian PSF with $\sigma_b = 0.707$

The binary and 4-ary PSFs for $\sigma_b = 1.0$ are:

Binary:

$$\begin{bmatrix} 0.00104 & 0.00347 & 0.00712 & 0.00905 & 0.00712 & 0.00347 & 0.00104 \\ 0.00347 & 0.0115 & 0.0236 & 0.0301 & 0.0236 & 0.0115 & 0.00347 \\ 0.00712 & 0.0236 & 0.0486 & 0.0617 & 0.0486 & 0.0236 & 0.00712 \\ 0.00905 & 0.0301 & 0.0617 & 0.0784 & 0.0617 & 0.0301 & 0.00905 \\ 0.00712 & 0.0236 & 0.0486 & 0.0617 & 0.0486 & 0.0236 & 0.00712 \\ 0.00347 & 0.0115 & 0.0236 & 0.0301 & 0.0236 & 0.0115 & 0.00347 \\ 0.00104 & 0.00347 & 0.00712 & 0.00905 & 0.00712 & 0.00347 & 0.00104 \end{bmatrix}, \tag{4.10}$$

4-ary:

$$\begin{bmatrix} 0.0000358 & 0.000363 & 0.00145 & 0.00229 & 0.00145 & 0.000363 & 0.0000358 \\ 0.000363 & 0.00368 & 0.0147 & 0.0232 & 0.0147 & 0.00368 & 0.000363 \\ 0.00145 & 0.0147 & 0.0589 & 0.0927 & 0.0589 & 0.0147 & 0.00145 \\ 0.00229 & 0.0232 & 0.0927 & 0.147 & 0.0927 & 0.0232 & 0.00229 \\ 0.00145 & 0.0147 & 0.0589 & 0.0927 & 0.0589 & 0.0147 & 0.00145 \\ 0.000363 & 0.00368 & 0.0147 & 0.0232 & 0.0147 & 0.00368 & 0.000363 \\ 0.0000358 & 0.000363 & 0.00145 & 0.00229 & 0.00145 & 0.000363 & 0.0000358 \end{bmatrix}. \tag{4.11}$$

The ML bounds for these two PSFs are shown in Fig. 4.6, where the 4-ary ML bound is computed using the 5×5 PSF. The binary ML bounds suggest that for this case we have to use 7×7 PSF. At BER of 10^{-8}, the SNR savings for 4-ary modulation is about 5dB.

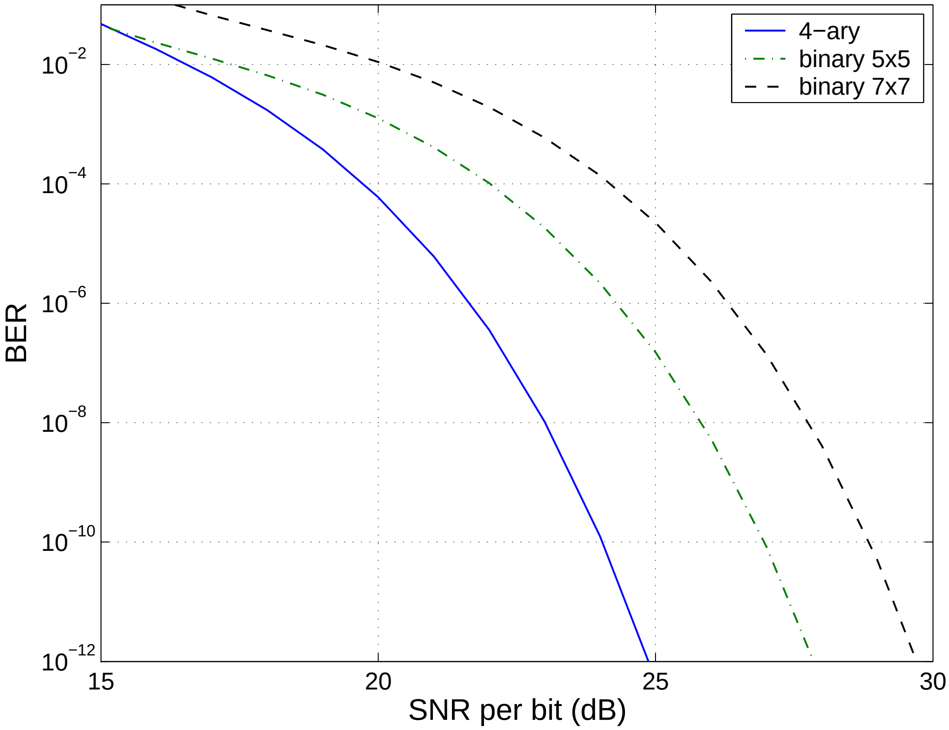

Figure 4.6: ML bound for Gaussian PSF with $\sigma_b = 1.0$

4.1.2 Sinc Square PSF

For sinc square channel with $\triangle/D = 0.9$,

$$h(k,l) = \int_{(k-1/2)/\delta}^{(k+1/2)/\delta} \int_{(l-1/2)/\delta}^{(l+1/2)/\delta} h(x,y)dxdy, \tag{4.12}$$

where $\delta = 1$ for 4-ary and $\delta = \sqrt{2}$ for binary, and

$$h(x,y) = \frac{1}{\triangle^2}\text{rect}(x/\triangle, y/\triangle) * \frac{1}{\sigma_b^2}\text{sinc}^2(x/\sigma_b, y/\sigma_b). \tag{4.13}$$

All the ML bounds computed for sinc square PSFs use 5×5 PSFs. The binary and 4-ary PSFs for $\sigma_b = 1.0$ are:

Binary:

$$\begin{bmatrix} 0.00040618 & 0.0039387 & 0.01079533 & 0.0039387 & 0.00040618 \\ 0.00393866 & 0.03819246 & 0.1046802 & 0.03819246 & 0.00393866 \\ 0.01079533 & 0.1046802 & 0.2869138 & 0.1046802 & 0.01079533 \\ 0.00393866 & 0.03819246 & 0.1046802 & 0.03819246 & 0.00393866 \\ 0.00040618 & 0.0039387 & 0.01079533 & 0.0039387 & 0.00040618 \end{bmatrix}, \tag{4.14}$$

4-ary:

$$\begin{bmatrix} 0.00023252 & 0.00196489 & 0.01049893 & 0.00196489 & 0.00023252 \\ 0.00196489 & 0.016604 & 0.0887198 & 0.016604 & 0.00196489 \\ 0.01049893 & 0.0887198 & 0.4740536 & 0.0887198 & 0.01049893 \\ 0.00196489 & 0.016604 & 0.0887198 & 0.016604 & 0.00196489 \\ 0.00023252 & 0.00196489 & 0.01049893 & 0.00196489 & 0.00023252 \end{bmatrix}. \tag{4.15}$$

The ML bounds for these two PSFs are shown in Fig. 4.7. In this case, the binary modulation performs better than 4-ary modulation by about 2dB.

The binary and 4-ary PSFs for $\sigma_b = 1.25$ are:

Binary:

$$\begin{bmatrix} 0.00054328 & 0.00515187 & 0.011295 & 0.00515187 & 0.00054328 \\ 0.00515187 & 0.0488544 & 0.10711 & 0.0488544 & 0.00515187 \\ 0.011295 & 0.10711 & 0.2348 & 0.10711 & 0.011295 \\ 0.00515187 & 0.0488544 & 0.10711 & 0.0488544 & 0.00515187 \\ 0.00054328 & 0.00515187 & 0.011295 & 0.00515187 & 0.00054328 \end{bmatrix}, \tag{4.16}$$

4-ary:

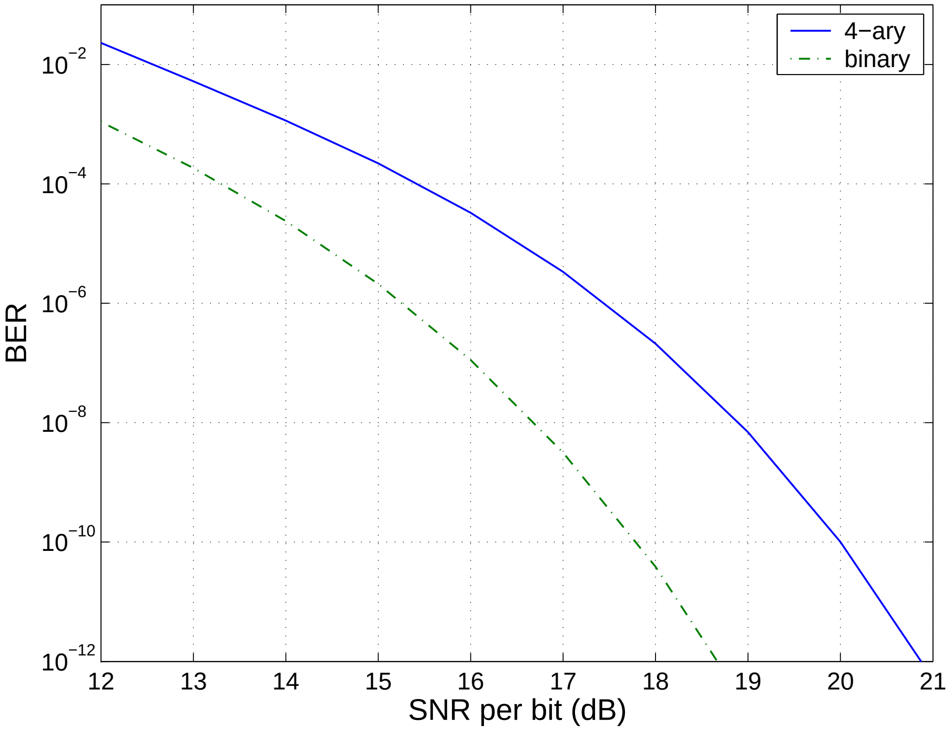

Figure 4.7: ML bound for sinc square PSF with $\sigma_b = 1.0$

$$\begin{bmatrix} 0.0003975 & 0.003181 & 0.01278 & 0.003181 & 0.0003975 \\ 0.003181 & 0.025457 & 0.102276 & 0.025457 & 0.003181 \\ 0.01278 & 0.102276 & 0.4109 & 0.102276 & 0.01278 \\ 0.003181 & 0.025457 & 0.102276 & 0.025457 & 0.003181 \\ 0.0003975 & 0.003181 & 0.01278 & 0.003181 & 0.0003975 \end{bmatrix}. \tag{4.17}$$

The ML bounds for these two PSFs are shown in Fig. 4.8. In this case, the binary modulation performs better than 4-ary modulation by about 0.5dB.

The binary and 4-ary PSFs for $\sigma_b = 1.5$ are:

Binary:

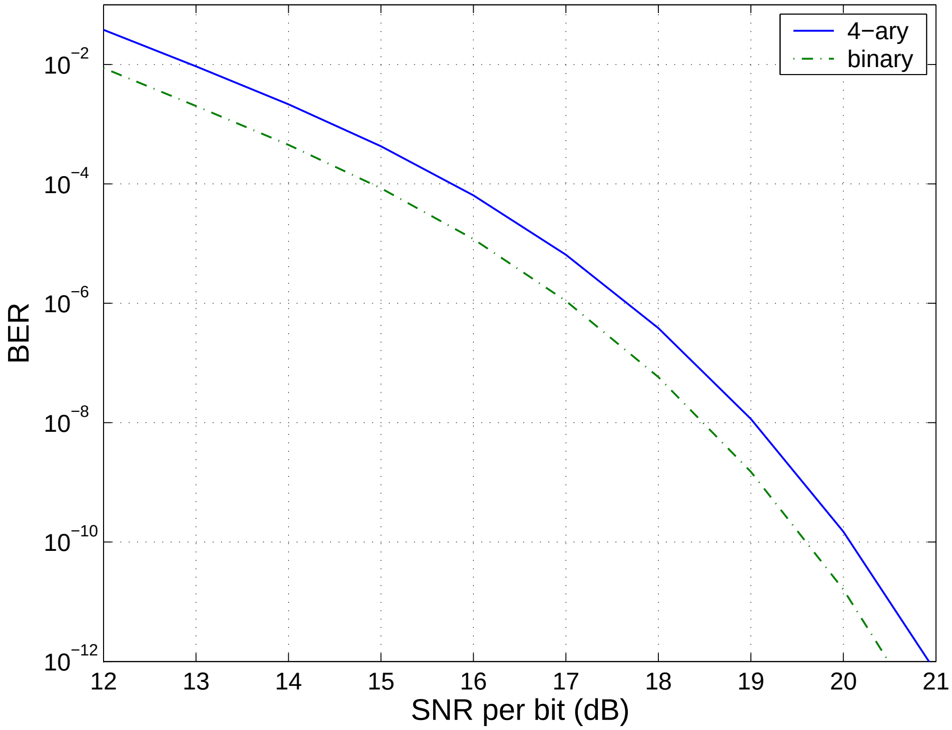

Figure 4.8: ML bound for sinc square PSF with $\sigma_b = 1.25$

$$\begin{bmatrix} 0.000942437 & 0.0070943 & 0.012981 & 0.0070943 & 0.000942437 \\ 0.0070943 & 0.0534031 & 0.09771737 & 0.0534031 & 0.0070943 \\ 0.012981 & 0.09771737 & 0.1788 & 0.09771737 & 0.012981 \\ 0.0070943 & 0.0534031 & 0.09771737 & 0.0534031 & 0.0070943 \\ 0.000942437 & 0.0070943 & 0.012981 & 0.0070943 & 0.000942437 \end{bmatrix}, \qquad (4.18)$$

4-ary:

$$\begin{bmatrix} 0.000397682 & 0.003637 & 0.0112027 & 0.003637 & 0.000397682 \\ 0.003637 & 0.0332656 & 0.10245928 & 0.0332656 & 0.003637 \\ 0.0112027 & 0.10245928 & 0.315578 & 0.10245928 & 0.0112027 \\ 0.003637 & 0.0332656 & 0.10245928 & 0.0332656 & 0.003637 \\ 0.000397682 & 0.003637 & 0.0112027 & 0.003637 & 0.000397682 \end{bmatrix}. \qquad (4.19)$$

The ML bounds for these two PSFs are shown in Fig. 4.9. In this case, the BERs for binary and 4-ary PSFs intersect at SNR around 16.5dB. At BER of 10^{-8}, the SNR savings for 4-ary modulation is about 0.6dB.

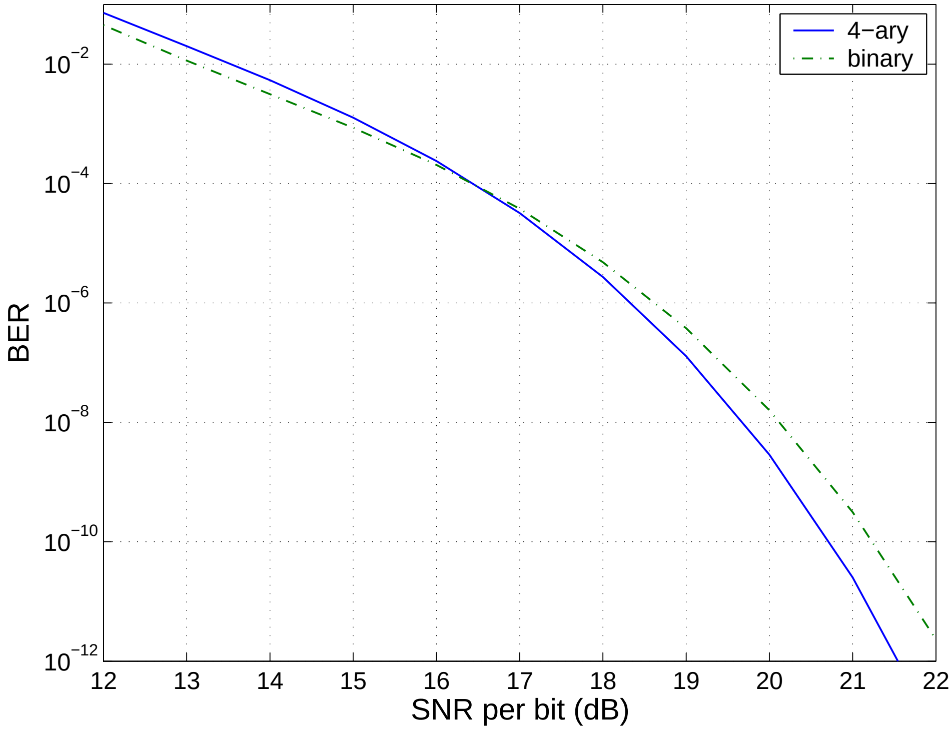

Figure 4.9: ML bound for sinc square PSF with $\sigma_b = 1.5$

4.2 The 4-ary i.i.d Source Detection for 2D ISI Channels

We consider a 2D ISI system as described in [3, 12], but the original symbols take values from the set {0, 1, 2, 3}.

For the 3×3 averaging mask, let $\mathbf{y}_k = [y_{k0}, y_{k1}, y_{k2}]$, and $\mathbf{u} = [u_{k0}, u_{k1}, u_{k2}]$. Consider the symbol $u \in \{0, 1, 2, 3\}$; the log-likelihood ratio (LLR) at the k-th stage can be defined as:

$$L_u(k) = \log\left(\frac{P(u_{k0} = u|\mathbf{y}_k, \tilde{\mathbf{u}})}{P(u_{k0} = u_{ref}|\mathbf{y}_k, \tilde{\mathbf{u}})}\right),$$

where $\tilde{\mathbf{u}} = [\tilde{u}_{k0}, \tilde{u}_{k1}, \tilde{u}_{k2}]$ is the estimation of symbol vector **u** from the other detector.

The extrinsic information input is

$$\tilde{L}_u(k) = \log\left(\frac{P(u_{k0} = u|\tilde{\mathbf{u}})}{P(u_{k0} = u_{ref}|\tilde{\mathbf{u}})}\right). \tag{4.20}$$

If we choose $u_{ref} = 0$, then $\tilde{L}_0(k) = 1$, and the conditional probability of the input symbol will be:

$$\begin{aligned} P(u_{k0} = 0|\tilde{\mathbf{u}}) &= \frac{1}{1 + \sum_{i=1}^{3} e^{\tilde{L}_i(k)}} \quad , \\ P(u_{k0} = u|\tilde{\mathbf{u}}) &= \frac{e^{\tilde{L}_u(k)}}{1 + \sum_{i=1}^{3} e^{\tilde{L}_i(k)}} \quad , \end{aligned} \tag{4.21}$$

where $u = 1, 2, 3$.

With the same definition for SNR, the 4-level system needs much higher SNR, which makes it difficult to implement MAP algorithm because of numerical representation problem (overflow). So Log-MAP algorithm [50] is used here, and it is equivalent to the true MAP.

The operator $\overset{*}{\max}$ is used in Log-MAP algorithm, which performs the following operation:

$$\overset{*}{\max_j}(a_j) \equiv \log\left[\sum_j e^{a_j}\right], \tag{4.22}$$

and it can be computed recursively, with initialization

$$\log(e^{\delta_1} + e^{\delta_2}) = \max(\delta_1, \delta_2) + \log(1 + e^{-|\delta_2 - \delta_1|}). \tag{4.23}$$

Suppose that $\delta = \log(e^{\delta_1} + \cdots + e^{\delta_{n-1}})$ is known, then,

$$\log(e^{\delta_1} + \cdots + e^{\delta_n}) = \log(e^{\delta} + e^{\delta_n}) = \max(\delta, \delta_n) + \log(1 + e^{-|\delta - \delta_n|}). \tag{4.24}$$

So for Log-MAP algorithm, from (4.21) the log of the conditional probability of the input symbol becomes:

$$\begin{aligned} \log\{P(u_{k0} = u|\tilde{\mathbf{u}})\} &= \tilde{L}_u(k) - \log\{1 + \sum_{i=1}^{3} e^{\tilde{L}_i(k)}\} \\ &= \tilde{L}_u(k) - \overset{*}{\max_j}(\tilde{L}_j(k)) \end{aligned} \tag{4.25}$$

Define $\lambda_k^{\mathbf{i}}(s) = P(\mathbf{u} = \mathbf{i}, S_k = s, \mathbf{y}_k)$, where $\mathbf{i} = [i_0, i_1, i_2], i_m \in \{0, 1, 2, 3\}$ is the input, and s is the state. Similarly with (1.10), we have

$$\log\{\lambda_k^{\mathbf{i}}(s)\} = \overset{*}{\max_{s'}}\{\alpha_{k-1}(s') + \gamma_{\mathbf{i}}(\mathbf{y}_k, s', s) + \beta_k(s)\}. \tag{4.26}$$

The $\alpha_k(s)$ and $\beta_k(s)$ are obtained through the forward and backward recursions, as

$$\alpha_k(s) = \overset{*}{\max_{s',\mathbf{i}}}\{\alpha_{k-1}(s') + \gamma_{\mathbf{i}}(\mathbf{y}_k, s', s)\} \tag{4.27}$$

$$\beta_k(s) = \overset{*}{\max_{s',\mathbf{i}}}\{\beta_{k+1}(s') + \gamma_{\mathbf{i}}(\mathbf{y}_{k+1}, s, s')\}. \tag{4.28}$$

with intial values

$$\alpha_0(s) = \begin{cases} 0, & s = S_0 \\ -\infty, & \text{otherwise} \end{cases} \qquad \beta_N(s) = \begin{cases} 0, & s = S_0 \\ -\infty, & \text{otherwise} \end{cases}.$$

The modified γ now is the following summation:

$$\begin{aligned} &\gamma_{\mathbf{i}}(\mathbf{y}_k, s', s) \\ &= \log\{p'(\mathbf{y}_k|\mathbf{u} = \mathbf{i}, S_k = s, S_{k-1} = s')\} + \log\{P(\mathbf{u} = \mathbf{i}|s, s')\} \\ &+ \log\{P(S_k = s|S_{k-1} = s')\} + \log\{P(\tilde{\mathbf{u}}|\mathbf{u} = \mathbf{i})\}. \end{aligned} \tag{4.29}$$

where $p'(\cdot)$ is the modified conditional channel PDF, for the given states s', s and input **u**, and $P(\mathbf{u} = \mathbf{i}|s, s')$ is 0 or 1 based on the trellis. $P(S_k = s|S_{k-1} = s')$ is a constant number for each branch and will be cancelled out when γ is used to compute LLRs.

The $\overset{*}{\max}$ operator is also used to compute the modified channel PDF,

$$\begin{aligned}&\log\{p'(\mathbf{y}_k|\mathbf{u}=\mathbf{i},S_k=s,S_{k-1}=s')\}=\log\{P\big(y_{k2}|u_{k0},u_{k1},u_{k2},s,s'\big)\}\\&+\overset{*}{\max_{\Omega_2}}\Bigg[\log\{P(\Omega_2)\}+\log\{P\big(y_{k1}|u_{k0},u_{k1},s,s',c_{\mathrm{sdf2}}(\Omega_2),\Omega_2\big)\}\\&+\overset{*}{\max_{\Omega_1}}\Bigg(\log\{P(\Omega_1)\}+\log\{P\big(y_{k0}|u_{k_0},s,s',c_{\mathrm{sdf1}}(\Omega_1,\Omega_2),\Omega_1,\Omega_2\big)\Bigg)\Bigg].\end{aligned} \tag{4.30}$$

The symbol LLR is then computed as:

$$L_u(k)=\overset{*}{\max_{s}}(\log\{\lambda_k^i(s)\}\text{ if }i_0=u)-\overset{*}{\max_{s}}(\log\{\lambda_k^i(s)\}\text{ if }i_0=0) \tag{4.31}$$

And we detect symbol u as $u=\operatorname*{argmax}_u(L_u(k))$, in other words, we detect the symbol u as the one which has the maximum value of $L_u(k)$.

For large x, $e^{-|x|}$ is approximately equal to 0. The Max-Log-MAP algorithm is a suboptimal algorithm especially at low SNR because it uses the max function to approximate the $\overset{*}{\max}$ operation. In our case, the SNR is relatively high, and the value of x in $e^{-|x|}$ is most likely very large, so we expect that the performance loss using Max-Log-MAP algorithm is not very big. This can be shown in Fig. 4.10, for both 32×32 and 64×64 signal size, the performances of Max-Log-MAP algorithm and Log-MAP algorithm are very close.

The complexity of the ISI detector will increase exponentially for 4-ary signals. For 2×2 mask with two inner products, the trellis has 16 states and 16 branches out of each state, while the binary case has 4 states and 4 branches out of each state. For 2×2 mask with three inner products, the trellis has 64 states and 64 branches out of each state, while the binary case has 8 states and 8 branches out of each state.

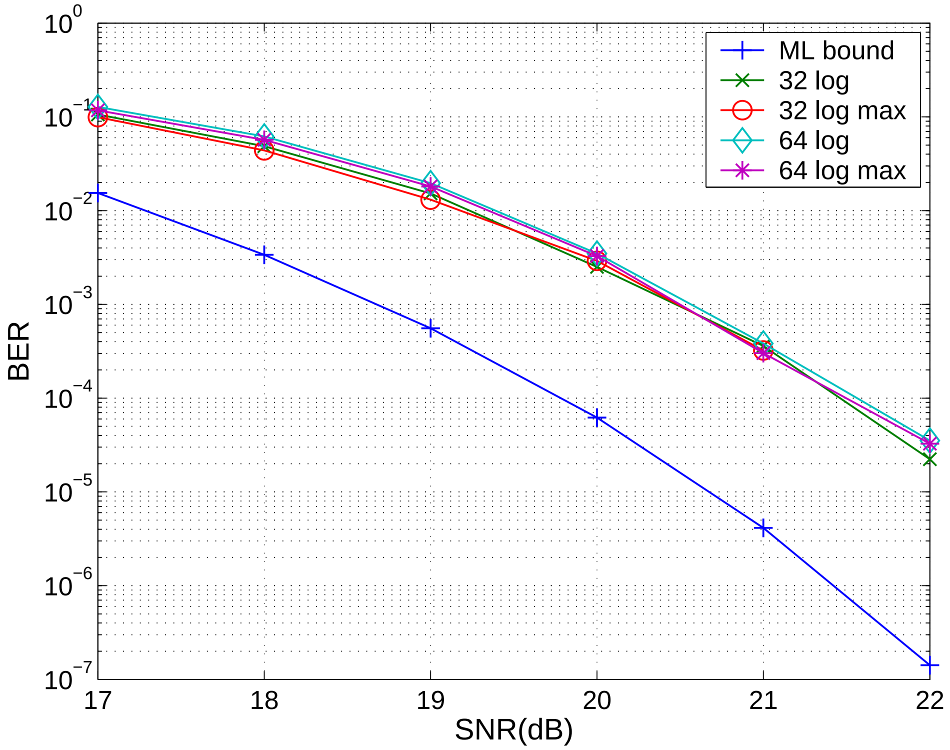

Figure 4.10: Test for Log-MAP and Max-Log-MAP algorithms for 2×2 mask.

For 3×3 mask, the trellis has 4096 states and 64 branches out of each state. To compute each branch metric, the soft feedback of 6 feedback symbols gives 4096 combinations. It takes too much time to simulate. So first we sort the 4096 feedbacks by their probabilities, then only use the N most probable combinations in (4.30) to run the simulation. The simulation of two blocks for 20dB after 6 iterations of 64×64 images are: top 25 case has 354 errors; top 50 case has 345 errors; top 100 case has 340 errors.

Fig. 4.11 shows the accumulated top 300 feedback probabilities for iteration 1, stage

k=3 and k=24 when SNR is 21dB. When k=3, top 160 can reach probability 0.99. When k=24, top 300 only reaches probability 0.41.

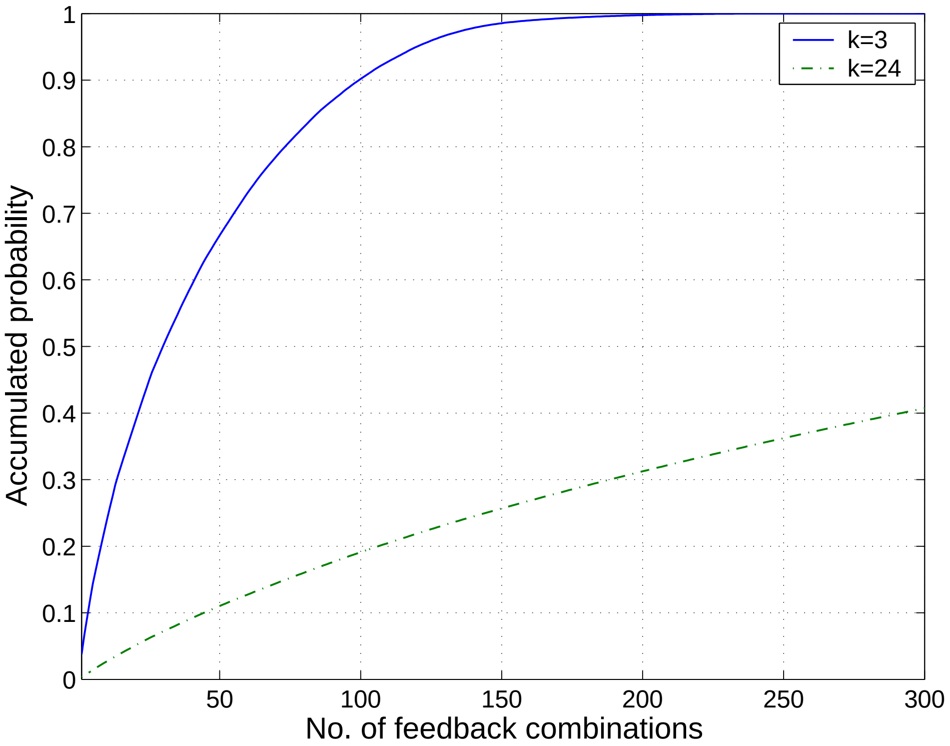

Figure 4.11: Probabilities of top 300 feedbacks for iteration 1, k=3 and k=24

The average accumulated probabilities of the top 300 feedbacks for 6 iteration are shown in Fig. 4.12. In iteration 1, the average accumulated probabilities for top 25 feedbacks are 0.31, for top 300 feedbacks are 0.79. In iteration 2, top 9 feedbacks can reach 0.99. After iteration 3, only the best feedback combination has probability other than 0.

Even the Max-Log-MAP algorithm takes too much time to simulate the 3×3 mask. So we use the same procedure for Max-Log-MAP algorithm and M-BCJR algorithm. Fig. 4.13 is the simulation results for the mask shown in (4.9). We can see after 6 iterations, using top

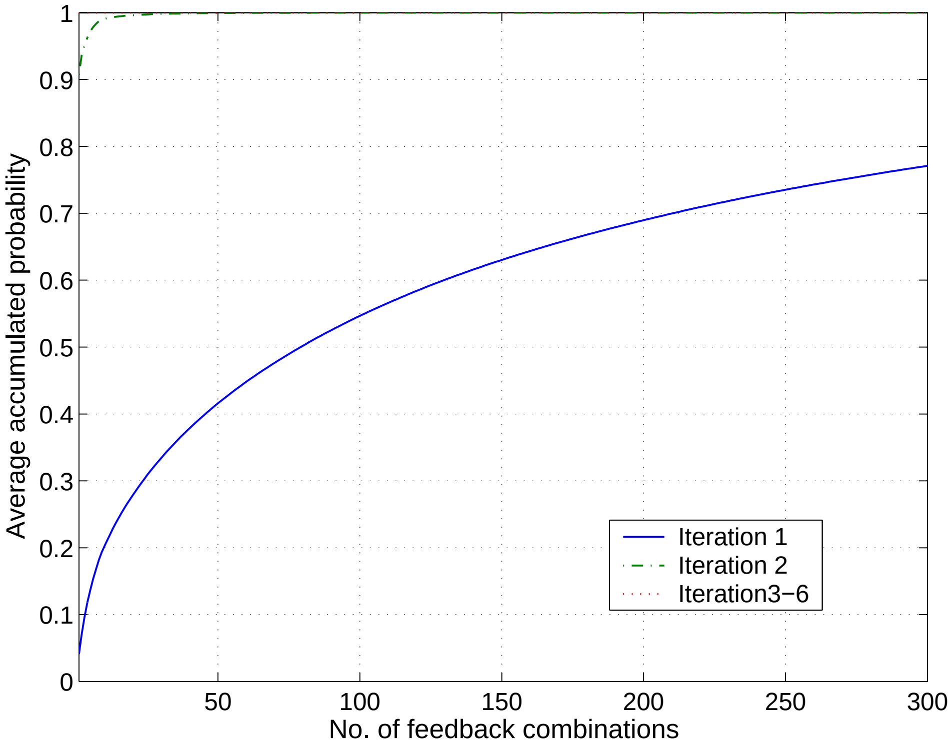

Figure 4.12: Average accumulated probabilities of top 300 feedbacks.

25 feedbacks and using top 50 feedbacks give us almost the same SER. We also include one point at 20dB for top 100, it gives almost the same results as top 25 and top 50. The curve labelled ’vary’ is the case where we use different number of feedbacks for each iteration: iteration 1 uses top 50, iteration 2 uses top 25, iteration 3 and 4 use top 5, iteration 5 and 6 use only top one feedback. At SER $= 10^{-3}$, it is about 3.5dB away from the ML bound. When M=2048, using top 75 feedbacks, there is about 1.6dB distance to the full trellis using top 25/50 feedbacks. The M-BCJR algorithm completely fails when M=25, using all 4096 feedbacks, which has the same complexity with top 25 using the full 4096 state trellis. When using top 50 feedbacks, M=1024 is about 3.6dB away from M=2048.

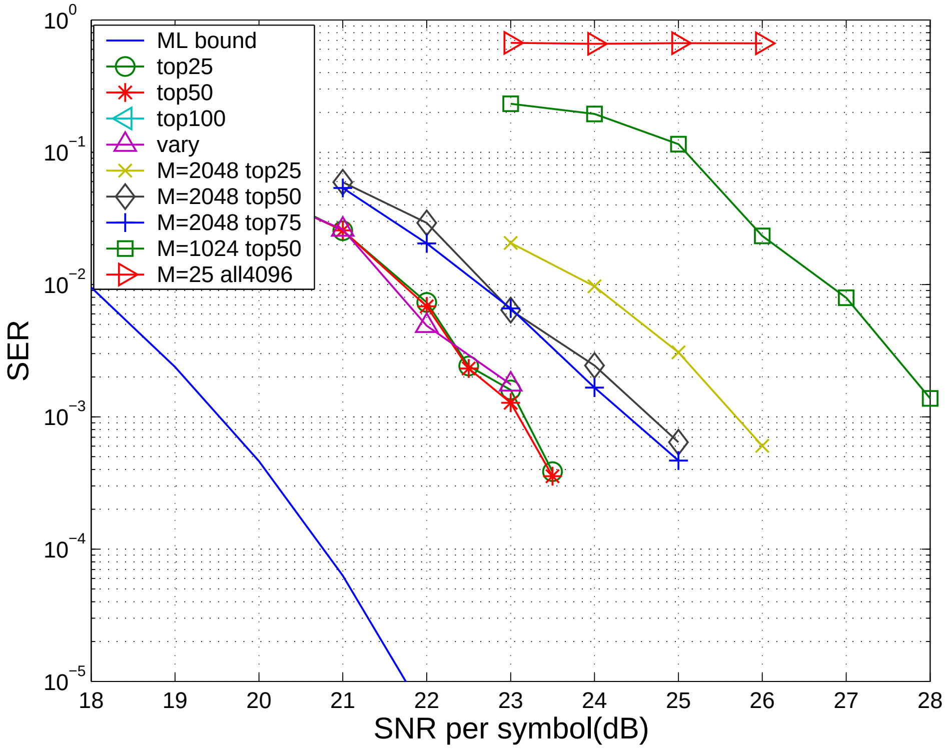

Figure 4.13: Simulation results for 4-ary 3x3 mask.

4.2.1 Set Partitioning Method

We want to investigate more for 4-ary or even M-ary signals. A set partitioning method is a possible choice [51]-[53]. Assume a M-PAM signal is used; the set partition is made in each symbol individually. For example, if M=4 and each symbol is partitioned into 2 subsets, then for 1D 1×2 mask, the full trellis has 4 states, the subset trellis has 2 states, and simulation results show that there is about 0.3dB performance deduction. For 2D 2×2 mask, the full trellis has 16 states and each state has 16 branches, while the subset trellis has 4 states and each state has 4 branches. We implement the algorithm using the Viterbi algorithm across rows with decision feedback from previously detected rows, similar to [7].

Fig. 4.14 shows the results for 256×256 signal using both full trellis and reduced state trellis; we can see that the performance deduction is also about 0.3dB.

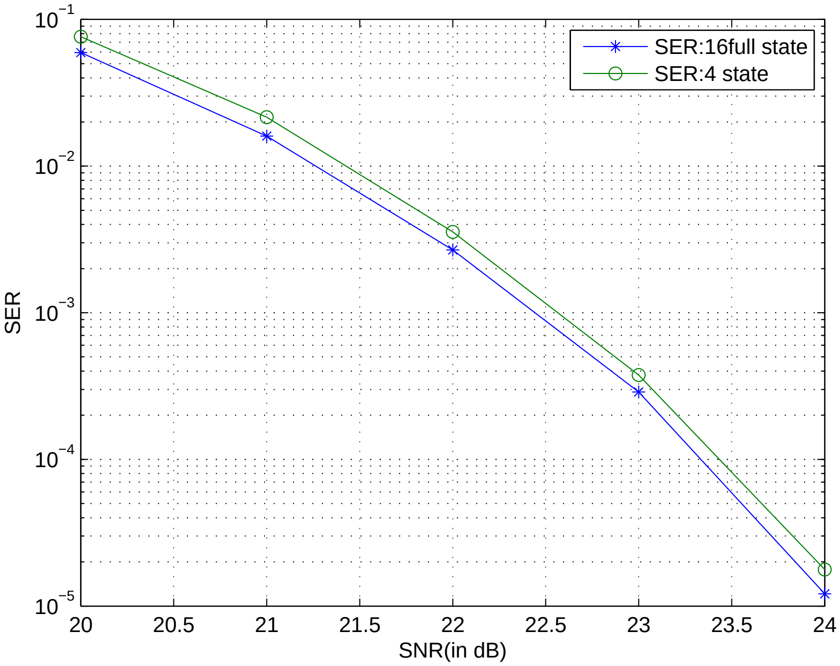

Figure 4.14: Simulation results for $2{\times}2$ averaging mask, gray level=4, signal size $256{\times}256$.

4.3 The Binary i.i.d Source Detection for Larger Masks

In section 4.2, we discussed 4-ary source detection for the mask shown in (4.9). For the same areal density, the equivalent binary PSF is shown in (4.8). Because this PSF is much more spread, we have to make the mask at least 5×5, rather than 3×3. Then if we define 4 columns as state, and 1 column as input, the trellis will have $2^{20} = 1048576$ states and $2^5 = 32$ branches out of each state. The 4 feedback rows will give $2^{20} = 1048576$ soft feedbacks. This huge trellis is impossible to simulate. We propose the following methods to simulate the 5×5 binary mask.

(1) Because the values in the corner of the mask are very small compared with other values, we can set them to 0 to reduce the number of states to $2^{18} = 262144$.

(2) Use the M-BCJR algorithm to reduce the number of states.

Chapter 5

Conclusion

5.1 Summary of Thesis Contribution

This dissertation has demonstrated that, if the input image to a 2D ISI channel has 2D correlation that can be modelled by a MRF, then significant SNR savings over previously proposed 2D-ISI detectors can be realized by employing a concatenated iterative decoder consisting of SISO 2D-ISI and MRF detectors, and that the SNR savings increase with the degree of source-image correlation. The techniques described in this dissertation have potential application in future-generation optical recording systems, which will employ 2D read/write heads. In practice, many source images destined for storage on such media are correlated; for example, uncompressed natural images are usually highly correlated, and most practical image-compression schemes leave residual correlation. This dissertation has also demonstrated that the proposed algorithm is quite robust to MRF parameter mismatch between the source image and the receiver, and that the simple first-order MRF is a very useful model for 2D-ISI reduction in natural binary images.

This dissertation has also developed and demonstrated a new reduced-state BCJR algorithm for detection on 1- and 2-dimensional finite-size ISI channels, that works especially well for center-weighted masks. This dissertation has also presented detailed performance comparisons between the newly proposed algorithm and two previously published algorithms, which point out the strengths and weaknesses of each algorithm. The 1D simulation results show that, for center-weighted masks, the proposed algorithm significantly outperforms the previously proposed MSM RS-SISO algorithm of [40]. However, the simulations also demonstrate that the M-BCJR algorithm of [41] gives by far the best performance for reduced-state 1D equalization, for both center-weighted and relatively "flat" ISI masks. The situation changes when the reduced-state algorithms are used in the row and column detectors of the 2D-ISI algorithm proposed in [3]. The newly proposed algorithm performs best for center weighted 2D masks with 0s in the corners, while the algorithm of [40] achieves the best performance for the averaging mask. The "Channel B" mask, based on sampling of a 2D Gaussian PDF [6], presented the most challenging test for all three algorithms; at high SNR, the best performing algorithm on "Channel B" was more than 2 dB away from the ML bound. We conclude that improved reduced-state algorithms are needed for 2D-ISI masks with Gaussian-like magnitude profiles.

In this dissertation, we compute equivalent masks for 4-ary and binary modulation with Guassian and Sinc square PSFs. To maintain the same areal density, the binary mask is wider than the corresponding 4-ary mask. Based on the ML bound, we find that for larger values of parameter σ_b, the BER of a 4-ary modulation can be better than that of the equivalent binary system. Reduced complexity algorithms for detection of 4-ary signals on 2D-ISI channels have also been proposed.

5.2 Future Work

The basic ideas of the detection of correlated sources on 2D-ISI presented in this dissertation should extend to more realistic image models and more practical scenarios. Algorithms that learn an appropriately accurate MRF model from the source image would allow practical implementation of joint 2D-ISI and MRF estimators in optical storage systems.

In this dissertation, we investigate the reduced-state BCJR algorithm for detection on 1- and 2-dimensional finite-size ISI channels, that works especially well for center-weighted masks. We would like to extend these results to other types of masks.

The detection of binary signals with larger size masks also needs to be investigated in the future, together with the 4-ary results in Chapter 4, to prove that the ML bound comparison can be realized in practice.

Bibliography

[1] W. Coene, "Coding and signal processing for two-dimensional optical storage (TwoDos)." Powerpoint presentation available at http://cm.bell-labs.com/cm/ms/events/WGIR04/pres/coene.ppt, Mar. 2004.

[2] G. T. Huang, "Holographic memory," *MIT Technology Review*, vol. 9, Sept. 2005. Online at http://www.inphase-tech.com.

[3] T. Cheng, B. J. Belzer, and K. Sivakumar, "Row-column soft-decision feedback algorithm for two-dimensional intersymbol interference," *IEEE Sig. Proc. Letters*, vol. 14, pp. 433–436, July 2007.

[4] John F. Heanue, Korhan Gürkan, and Lambertus Hesselink, "Signal detection for page-access optimal memories with intersymbol interference," *Applied Optics*, vol. 35, no. 14, pp. 2431–2438, May 1996.

[5] R. Krishnamoorthi, "Two-dimensional Viterbi like algorithms," M.S. thesis, Univ. Illinois at Urbana Champaign, 1998.

[6] X. Chen and Keith M. Chugg, "Near-optimal data detection for two-dimensional ISI/AWGN channels using concatenated modeling and iterative algorithms," in *Proc. IEEE International Conference on Communications, ICC'98*, 1998, pp. 952–956.

[7] C. Miller, B.R. Hunt, M.A. Neifeld, and M.W.Marcellin, "Binary image reconstruction via 2-D Viterbi search," in *Proc. IEEE International Conference on Image Processing, (ICIP97)*, 1997, vol. 1, pp. 181–184.

[8] M. Marrow and J. K. Wolf, "Iterative detection of 2-dimensional ISI channels," in *Proc. Info. Theory Workshop*, Paris, France, Mar./Apr. 2003, pp. 131–134.

[9] M. Marrow and J. K. Wolf, "Equalization and detection of 2-D ISI channels." Slide presentation available at http://cmrr-wolf08.ucsd.edu/~mmarrow/, May 2003.

[10] Y. Wu, J. A. O'Sullivan, N. Singla, and Ronald S. Indeck, "Iterative detection and decoding for separable two-dimensional intersymbol interference," *IEEE Trans. Magnetics*, vol. 39, no. 4, pp. 2115–2120, July 2003.

[11] O. Shental, A.J. Weiss, N. Shental, and Y. Weiss, "Generalized belief propagation receiver for near-optimal detection of two-dimensional channels with memory," in *IEEE Information Theory Workshop*, 24-29 Oct. 2004, pp. 225 – 229.

[12] T. Cheng, B. J. Belzer, and K. Sivakumar, "Image deblurring with iterative row-column soft-decision feedback algorithm," in *Proc. 39th Conf. on Info. Sci. and Systems (CISS2005)*, Johns-Hopkins U., Baltimore, MD, Mar. 2005, CD-ROM.

[13] P. M. Njeim, T. Cheng, B. J. Belzer, and K. Sivakumar, “Image detection in 2D intersymbol interference with iterative soft-decision feedback zig-zag algorithm,” in *Proc. 43rd annual Allerton Conf. on Comm., Computing, and Control*, Univ. of Illinois, Urbana-Champaign, IL, Sept. 2005, CD-ROM.

[14] B. Vasic and E. M. Kurtas, *Coding and Signal Processing for Magnetic Recording Systems*, Boca Raton: CRC Press, 2005.

[15] Wikipedia, “Multilevel recording,” http://en.wikipedia.org/wiki/MultiLevel_Recording, Apr. 2006.

[16] Lina Fagoonee, Wim M. J. Coene, and Abdolhosein Moinian, “Nonlinear signal-processing model for signal generation in multilevel two-dimensional optical storage,” *Optics Letters*, vol. 29, no. 4, pp. 385–387, Feb. 2004.

[17] Abdolhosein Moinian, Lina Fagoonee, and Bahram Honary, “Low complexity symbol detection method for multilevel 2-d optical storage based on a linear channel model,” *Optical Engin*, vol. 44, no. 10, pp. 105201, Oct. 2005.

[18] J. Xiao, G. Qi, P. She, R. Liu, and D. Xu, “Multilevel optical data recording methods on phase-change media,” *Chinese Physics*, vol. 12, no. 11, pp. 1241–1245, Nov. 2003.

[19] United States Patent, “Multilevel record modulator and demodulator,” http://www.freepatentsonline.com/6778483.html, Apr. 2006.

[20] V. Vadde and B. V. K. Vijaya Kumar, “Channel modeling and estimation for intrapage equalization in pixel-matched volume holographic data storage,” *Applied Optics*, vol. 38, no. 20, pp. 4374–4386, 1999.

[21] M. A. Neifeld, K. M. Chugg, and B. M. King, “Parallel data detection in page-oriented optical memory,” *Optics Letters*, vol. 21, no. 18, pp. 1481–1483, Sept. 1996.

[22] Brian M. King and Mark A. Neifeld, “Parallel detection algorithm for page-oriented optical memories,” *Applied Optics*, vol. 37, no. 26, pp. 6275–6298, 1998.

[23] Keith M. Chugg, “Performance of optimal digital page detection in a two-dimensional ISI/AWGN channel,” in *Proc. Asilomar Conf. on Signals, Systems and Comp.*, Nov. 1996, pp. 958–962.

[24] M. R. Banham and A. K. Katsaggelos, “Digital image restoration,” *IEEE Sig. Proc. Mag.*, pp. 24–41, Mar. 1997.

[25] P. Ellingsen, O. Ytrehus, and P. Siegel, “Enhanced decoding by error detection on a channel with correlated 2-dimensional errors,” in *IEEE Information Theory Workshop*, Oct. 2004, pp. 17–21.

[26] John K. Goutsias, “Unilateral approximation of Gibbs random field images.,” *CVGIP: Graphical Model and Image Processing*, vol. 53, no. 3, pp. 240–257, 1991.

[27] J. K. Goutsias, “Mutually compatible Gibbs random fields,” *IEEE Transactions on Information Theory*, vol. 35, no. 6, pp. 1233–1249, Nov. 1989.

[28] S. Geman and D. Geman, "Stochastic relaxation, Gibbs distributions, and the Bayesian restoration of images," *IEEE Trans. Pattern Analysis Mach. Intell.*, vol. 6, pp. 721–741, Nov. 1984.

[29] J. Kliewer, N. Gortz, and A. Mertins, "Iterative source-channel decoding with Markov random field source models," *IEEE Trans. Sig. Proc.*, vol. 54, pp. 3688–3701, Oct. 2006.

[30] J. Kliewer, N. Gortz, and A. Mertins, "On iterative source-channel image decoding with Markov random field source models," in *Proceedings of IEEE International Conference on Acoustics, Speech, and Signal Processing, 2004. (ICASSP '04),* May 2004, vol. 4, pp. iv–661–iv–664.

[31] A. Mertins, "Image recovery from noisy transmission using soft bits and Markov random field models," *Optical Engineering*, vol. 42, no. 10, pp. 2893–2899, Oct. 2003.

[32] J. Wang, L.-L. Yang, and L. Hanzo, "Iterative channel equalization, channel decoding and source decoding," in *Proc. 2005 61st IEEE Veh. Tech. Conf.*, May/June 2005, vol. 1, pp. 518–522.

[33] L.-L. Yang, R. Maunder J. Wang, and L. Hanzo, "Iterative equalization and source decoding for vector quantized sources," in *Proc. 2006 IEEE 63rd Veh. Tech. Conf.*, May 2006, vol. 5, pp. 2349–2353.

[34] G. Caire and M. Fresia, "Joint source-channel coding: a practical approach and an implementation example," in *Proc. ITA 2007 Workshop on Information Theory and its Applications*, U. of California San Diego, Jan 2007, vol. 5, pp. 2349–2353.

[35] G. D. Forney, "The Viterbi algorithm," in *Proceedings of the IEEE*, 1973, vol. 61, pp. 268–278.

[36] L. R. Bahl, J. Cocke, F. Jelinek, and J. Raviv, "Optimal decoding of linear codes for minimizing symbol error rate," *IEEE Trans. Inform. Theory*, vol. 20, pp. 284–287, Mar. 1974.

[37] P. Thiennviboon, G. Ferrari, and K. M. Chugg, "Generalized trellis-based reduced-state soft-input/soft-output algorithms," in *IEEE International Conference on Communications, 2002. ICC 2002*, 2002, vol. 3, pp. 1667–1671.

[38] L. Huang, G.Mathew, and T.C.Chong, "Reduced complexity Viterbi detection for two-dimensional optical recording," *IEEE Transactions on Consumer Electronics*, vol. 51, no. 1, pp. 123–129, Feb. 2005.

[39] G. Colavolpe, G. Ferrai, and R. Raheli, "Reduced-state BCJR-type algorithms," *IEEE Jour. on Sel. Areas in Commun.*, vol. 19, pp. 848–859, May 2001.

[40] X. Chen and K. M. Chugg, "Reduced-state soft-input/soft-output algorithms for complexity reduction in iterative and non-iterative data detection," in *Proc. 2000 IEEE*

International Conf. on Commun. (ICC 2000), New Orleans, LA, June 2000, vol. 1, pp. 6–10.

[41] C. Fragouli, N. Seshadri, and W. Turin, "Reduced-trellis equalization using the M-BCJR algorithm," *Wireless Commun. and Mobile Computing*, vol. 1, pp. 397–406, July 2001.

[42] Y. Zhu, T. Cheng, K. Sivakumar, and B. J. Belzer, "Detection of Markov random fields on two-dimensional intersymbol interference channels," in *Proc. 44th Annual Allerton Conf. on Comm., Computing, and Control*, Univ. of Illinois, Urbana-Champaign, IL, Sept. 2006.

[43] Y. Zhu, T. Cheng, K. Sivakumar, and B. J. Belzer, "Markov random field detection on two-dimensional intersymbol interference channels," *IEEE Transactions on Signal Processing*, vol. 56, pp. 2639–2648, July 2008.

[44] Y. Zhu, B. J. Belzer, and K. Sivakumar, "Reduced state BCJR algorithms for one- and two-dimensional equalization," in *IEEE International Conference on Acoustics, Speech and Signal Processing*, Las Vegas, NV, Mar./Apr. 2008, pp. 3201–3204.

[45] C. Berrou and A. Glavieux, "Near optimum error correcting coding and decoding: turbo-codes," *IEEE Trans. Commun.*, vol. 44, no. 10, pp. 1261 – 1271, Oct. 1996.

[46] Taikun Cheng, *Equalization And Coding For The Two-Dimensional Intersymbol Interference Channel*, Ph.D. thesis, Washington State University, 2007.

[47] G. R. Cross and A. K. Jain, “Markov random field texture models,” *IEEE Trans. Pattern Analysis and Machine Intelligence*, vol. PAMI-5, pp. 25–39, Jan. 1983.

[48] M. Antonini, M. Barlaud, P. Mathieu, and I. Daubechies, “Image coding using wavelet transform,” *IEEE Trans. Im. Proc.*, vol. 1, pp. 205–220, 1992.

[49] D. Fertonani, A. Barbieri, and G. Colavolpe, “Reduced-complexity BCJR algorithm for turbo equalization,” *IEEE Trans. on Communications*, vol. 12, pp. 2279–2287, Dec. 2007.

[50] P. Robertson, E. Villebrun, and P. Hoeher, “A comparison of optimal and sub-optimal map decoding algorithmsoperating in the log domain,” in *IEEE International Conference on Communications, 1995. ICC 95*, June 1995, vol. 2, pp. 1009–1013.

[51] M. V. Eyuboğlu and S. U. H. Qureshi, “Reduced-state sequence estimation with set partitioning and decision feedback,” *IEEE Trans. Commun.*, vol. 36, no. 1, pp. 13–20, Jan. 1988.

[52] L. Reggiani, G. Tartara, and G.M. Maggio, “A reduced-state soft input soft output algorithm based on state partitioning,” in *IEEE Global Telecommunications Conference*, San Antonio, TX, Nov. 2001, vol. 2, pp. 906–910.

[53] M. V. Eyuboglu and S. U. H. Qureshi, “Reduced-state sequence estimation for coded modulation of intersymbol interference channels,” *IEEE Journal on Selected Areas in Communications*, vol. 7, no. 6, pp. 989–995, Aug. 1989.